fibers

MDPI

Review

Recent Developments in Micro-Structured Fiber Optic Sensors

Yanping Xu [1], Ping Lu [2], Liang Chen [1] and Xiaoyi Bao [1,*]

[1] Department of Physics, University of Ottawa, 25 Templeton Street, Ottawa, ON K1N 6N5, Canada; erisonxu@gmail.com (Y.X.); liang.chen@uottawa.ca (L.C.)
[2] National Research Council Canada, 100 Sussex Drive, Ottawa, ON K1A 0R6, Canada; ping.lu@nrc-cnrc.gc.ca
* Correspondence: xiaoyi.bao@uottawa.ca; Tel.: +1-613-562-5800 (ext. 6911)

Academic Editor: Torsten Frosch
Received: 11 August 2016; Accepted: 25 October 2016; Published: 10 January 2017

Abstract: Recent developments in fiber-optic sensing have involved booming research in the design and manufacturing of novel micro-structured optical fiber devices. From the conventional tapered fiber architectures to the novel micro-machined devices by advanced laser systems, thousands of micro-structured fiber-optic sensors have been proposed and fabricated for applications in measuring temperature, strain, refractive index (RI), electric current, displacement, bending, acceleration, force, rotation, acoustic, and magnetic field. The renowned and unparalleled merits of sensors-based micro-machined optical fibers including small footprint, light weight, immunity to electromagnetic interferences, durability to harsh environment, capability of remote control, and flexibility of directly embedding into the structured system have placed them in highly demand for practical use in diverse industries. With the rapid advancement in micro-technology, micro-structured fiber sensors have benefitted from the trends of possessing high performance, versatilities and spatial miniaturization. Here, we comprehensively review the recent progress in the micro-structured fiber-optic sensors with a variety of architectures regarding their fabrications, waveguide properties and sensing applications.

Keywords: optical fiber; fiber-optic sensors; micro-structured optical fiber; optical microfiber; micro-machined optical fiber

1. Introduction

Fiber-optic sensors have attracted intensive attentions during the past decades due to their unparalleled advantages over the conventional sensors such as immunity to electromagnetic interference, capability of measuring multiple measurands, high resolution, high accuracy, small footprint (~μm), long-distance sensing, ability for high temperature measurement (>300 °C), ability of sensor networking, etc. [1–5]. Many of the fiber-optic sensors have been successfully commercialized and widely practically applied for health and safety monitoring of composite materials, large civil engineering structures, quantitative chemical process, and structural health monitoring. The rapid development in the micro-technology imposes more merits on the novel micro-structured fiber-optic sensors such as faster response, smaller size, higher sensitivity, and lower power consumption, which stimulates great efforts for miniaturization of the fiber-optic components and devices. The growing interest for this exciting area of scientific research has given rise to a lot of new designs and fabrication techniques at a fast pace in recent years. Compared with conventional fiber-optic point sensors, for example, the Mach-Zehnder interferometer (MZI) with cumbersome structures consisting of two beams of optical fibers or the extrinsic Fabry-Perot interferometer (FPI) by packaging two fiber ends together, the micro-structured fiber optic sensors are easily able to realize the interferometric schemes with an in-fiber configuration through tapering, laser micro-machining and so on, which makes the sensor more compact and reliable. Furthermore, the enhancement of the evanescent fields in the micro-structured fiber optic sensors enables much higher sensitivity to the refractive index (RI) measurements than the conventional long-period gratings inscribed in normal optical fibers.

The micro-structured optical fiber sensors, as we interpret them here, refer to fiber sensors which are either micro-machined or micro-manipulated in the scale of micron level in an optical fiber or manufactured in a microfiber such as tapered fiber structures. In general, there are two types of sensor configurations, namely fiber-optic interferometers and gratings [6–10]. Fiber-optic interferometers mainly include MZI, Michelson interferometer (MI), and FPI. Most micro-structured MZIs and MIs rely on the coupling between the fundamental mode guided in the fiber core and the higher-order modes due to their phase difference induced by the different effective refractive indices and path lengths [11–13]. The excitation and coupling back of the higher-order modes are realized by the micro-structured modification on the devices. The micro-structured FPI devices are usually realized by removing part of the fiber material using chemical etching and laser ablation so as to form an air-filled cavity in the fiber [14,15]. The reflections on the two formed mirrors of the cavity provide the interference of light and hence could be utilized for sensing applications. Micro-structured fiber gratings mainly include the microfiber-based fiber Bragg grating (FBG), long period grating (LPG) and the recently-emerged random gratings. Due to the enhanced evanescent field owing to the use of microfibers, these FBGs or LPGs respond to the external disturbances with an increased sensitivity and higher precision. Low optical loss, excellent mechanical flexibility, tight optical confinement and large evanescent fields could be achieved with these devices, which make them a novel micro-structured platform for various optical sensing applications such as in process control of manufacturing industries, protection of ecosystems, quality control in food industries, biomedical and biochemical applications, etc.

The micro-structured optical fiber sensors have been applied to a variety of physical, chemical, and biological optical sensing areas to date [16–18]. Fast response, high sensitivity, and high accuracy have been demonstrated among these micro-structured optical fiber sensors. This paper reviews various micro-structured optical fiber sensors that have been designed and manufactured in different sensing configurations, their working principles, as well as the typical applications. The paper is arranged as follows: the introduction is presented in Section 1; followed by the fundamental physics and principles in Section 2; Abrupt taper structure and long taper structure will be introduced in Sections 3 and 4; Resonator-type micro-structure and micro-machined devices will be covered in Sections 5 and 6; the grating-based microstructures and some mode-mismatched and hybrid micro-structures will be described in Sections 7 and 8; In Sections 9 and 10 we will provide the future prospect and conclusions of the paper.

2. Fundamental Physics of Micro-Structured Fiber Optic Sensors

2.1. Interferometer-Type Micro-Structured Fiber Optic Sensors

Most interferometer-type micro-structured fiber optic sensors are based on the couplings between the fundamental core mode and the higher-order cladding modes guided along the microstructures. Thus, there is need to analyze the fundamental physics of the properties of the micro-structured waveguides in terms of the evolution of core mode and cladding modes.

To investigate how light propagates along the fiber in the form of core mode and cladding modes, the wave equation is needed for analysis. A regular optical fiber is normally a weakly guided waveguide which supports light modes propagating along the fiber in terms of linearly polarized modes ($\mathrm{LP}_{\upsilon\mathrm{m}}$). The propagation constants for LP modes are obtained by accurately solving a set of scalar wave equations. The electric fields that propagate in the z-direction along the fiber satisfy the scalar wave equation, which is given in cylindrical coordinates by:

$$(\frac{\partial^2}{\partial r^2}+\frac{1}{r}\frac{\partial}{\partial r}+\frac{1}{r^2}\frac{\partial^2}{\partial \phi^2}+k^2n^2-\beta^2)\psi=0 \tag{1}$$

where ψ represents the electric or magnetic field, k is the free space wavenumber, n is the RI and β is the propagation constant with the expression $\beta = kn_{eff}$.

Firstly, we calculate the effective RI of the core mode. The weak-guidance approximation is applied due to a slight variation between the core and cladding indices. Thus, the propagation constants for the local LP modes are obtained accurately by solving a set of scalar wave equations with continuity of the solution and its first derivative at the core-cladding interface along the micro-structured fiber.

The effective RI of core mode n_{eff} satisfies $n_{cl} < n_{eff} < n_{co}$, we consider the bounded solution with core-cladding interface. The solution of Equation (1) is given as:

$$\psi = \begin{cases} AJ_v(u_1 r)\mathrm{e}^{iv\phi} & if\ 0 \le r \le \rho \\ CK_v(wr)\mathrm{e}^{iv\phi} & if\ \rho \le r \le \rho_{cl} \end{cases} \tag{2}$$

where u_1 and w are defined as:

$$u_1 = k(n_{co}^2 - n_{eff}^2)^{\frac{1}{2}} \tag{3}$$

$$w = k(n_{eff}^2 - n_{cl}^2)^{\frac{1}{2}} \tag{4}$$

A and C are constants, ρ and ρ_{cl} are core and cladding radii, respectively. J_v and K_v are the vth order Bessel function of the first kind and the modified Bessel function of the second kind, respectively. Continuity of electromagnetic field ψ and its first derivative at the core boundary $r = \rho$ relates the values of A and C and leads to a set of eigenvalue equations as [19]:

$$u_1 \frac{J_{v+1}(u_1\rho)}{J_v(u_1\rho)} = w\frac{K_{v+1}(w\rho)}{K_v(w\rho)} \tag{5}$$

The eigenvalues obtained from Equation (5) are labeled as β_{vm} with $v = 0, 1, 2, \ldots$, $m = 1, 2, 3, \ldots$, where the subscript m indicates the mth root of Equation (5). The modes are designated $\mathrm{LP}_{\upsilon\mathrm{m}}$.

The effective RI of cladding mode n_{eff} satisfies $n_{air} < n_{eff} < n_{cl}$, we consider the bounded solutions with the core-cladding and cladding-air interfaces. The solution of Equation (1) is solved based on a three-layer step-index fiber model [20] with dispersion relation, which is given as:

$$\psi = \begin{cases} AJ_v(u_1 r)e^{iv\phi} & \text{if } 0 \le r \le \rho \\ [BJ_v(u_1 r) + CY_v(u_2\rho)]\mathrm{e}^{iv\phi} & \text{if } \rho \le r \le \rho_{cl} \\ DK_v(w_3 r)\mathrm{e}^{iv\phi} & \text{if } r \ge \rho_{cl} \end{cases} \tag{6}$$

where the modal parameters are defined as:

$$u_1 = k(n_{co}^2 - n_{eff}^2)^{\frac{1}{2}} \tag{7}$$

$$u_2 = k(n_{cl}^2 - n_{eff}^2)^{\frac{1}{2}} \tag{8}$$

$$w_3 = k(n_{eff}^2 - n_{air}^2)^{\frac{1}{2}} \tag{9}$$

A, B, C and D are constants, Y_v is the vth order Bessel function of the second kind. Similar to the core mode, the continuity of electromagnetic fields and their derivatives at the two interfaces results in a set of equations relating the values of A, B, C and D and provides the eigenvalue equations from consistency conditions. The calculated eigenvalues are the cladding modes $\mathrm{LP}_{\upsilon\mathrm{m}}$ ($v > 0$).

The effective RI of core mode n_{eff} decreases with the reduction in the diameter of the fiber core. When n_{eff} approaches the RI of the cladding, the core mode will be coupled to the cladding modes with $n_{air} < n_{eff} < n_{cl}$ propagating along both core and cladding regions. This is called the "core to cladding-mode transition" or "core-mode cutoff" [21]. The core-cladding transition value $V_{core/cladding}$ is given by [22]:

$$V_{core/cladding} = \frac{2\pi}{\lambda}\frac{\rho_{cl}}{S}\sqrt{n_{co}^2 - n_{cl}^2} \cong \sqrt{\frac{2}{\ln S}}(1 + \frac{0.26}{\ln S})^{-\frac{1}{2}} \tag{10}$$

where S is the ratio of cladding to core diameter. Theoretically, when using the parameter of a standard single mode fiber, the fundamental core mode is split into several cladding modes when the fiber is tapered down to a cladding diameter of 51.1 μm.

The mode field patterns of excited cladding modes in the micro-structured fiber devices are determined by the azimuthal symmetry of the light steering elements. If they are axisymmetric, only the modes with the same azimuthal symmetry (LP_{0m}) could be excited. The LP_{02} mode usually dominates among the excited symmetric modes. While in the non-axisymmetric case, the energy of the fundamental mode LP_{01} will mostly be coupled to the non-axisymmetric mode with closest effective refractive index, i.e., the LP_{11} mode. A coupling coefficient η is introduced to characterize energy conversion from the LP_{01} mode to high-order modes and it is generally given as:

$$\eta = \frac{|\iint \psi_{01}(x,y)\psi_{vm}^{*}(x,y)\mathrm{d}x\mathrm{d}y|^2}{\iint \psi_{01}\psi_{01}^{*}\mathrm{d}x\mathrm{d}y \iint \psi_{vm}\psi_{vm}^{*}\mathrm{d}x\mathrm{d}y} \tag{11}$$

where ψ_{01} is the electromagnetic field of LP_{01}, ψ_{vm} are the electromagnetic fields of cladding modes.

The couplings between the fundamental core mode and higher-order cladding modes laid the foundation for the working principles of the micro-structured fiber optic sensors. The phase difference between the fundamental core mode LP_{01} and a given cladding mode LP_{ij} propagating through an interferometer of length L at the operating wavelength λ could be derived with their optical path length (OPL) difference:

$$\Delta\Phi_{ij} = \Phi_{01} - \Phi_{ij} = \frac{2\pi L}{\lambda}(n_{eff}^{01} - n_{eff}^{ij}) = \frac{2\pi\Delta n_{eff}^{ij} L}{\lambda} \tag{12}$$

where $\Delta n^{ij}{}_{eff}$ is the difference between the effective refractive indices of the two modes. When the phase difference between the fundamental core mode LP_{01} and the cladding mode LP_{ij} is equal to $2m\pi$, an interference maximum could be observed in the transmission spectrum, and the m-order peak wavelength is located at:

$$\lambda_m^{ij} = \frac{\Delta n_{eff}^{ij} L}{m} \tag{13}$$

The interfering intensity of the coupling between the core mode and the cladding modes is expressed by:

$$I = I_{01} + \sum_{ij} I_{ij} + 2\sum_{ij}\sqrt{I_{01}I_{ij}}\cos(\frac{2\pi\Delta n_{eff}^{ij} L}{\lambda}) \tag{14}$$

Since $O(\Delta n^{ij}{}_{eff}) \approx 10^{-3}$, $L \approx 10^{-1}$ m, and $O(\lambda) \approx 10^{-6}$ m, then $O(\Delta n^{ij}{}_{eff}L/\lambda) \approx 10^2$. Thus, the optical path length difference $\Delta OPL = \Delta n^{ij}{}_{eff}L$ between the core mode and the cladding modes is large enough that $\Delta n^{ij}{}_{eff}L >> \lambda$ and $m >> 1$, the separation between the neighboring maxima in the interference spectrum could be approximated to:

$$\Delta\lambda_{ij} = \lambda_{m-1}^{ij} - \lambda_m^{ij} \approx \frac{\lambda_0^2}{\Delta n_{eff}^{ij} L} \tag{15}$$

where λ_0 is the center wavelength in the given spectral range. The interference between the fundamental core mode and a cladding mode LP_{ij} will therefore lead to an oscillating interference pattern with a period of $\Delta\lambda_{ij}$ corresponding to the intensity peak at a spatial frequency ξ_{ij} which can be expressed as:

$$\xi_{ij} = \frac{1}{\Delta\lambda_{ij}} \approx \frac{\Delta n_{eff}^{ij} L}{\lambda_0^2} \tag{16}$$

If the environmental parameters such as surrounding RI, temperature and strain change, the difference in the effective refractive indices between the core mode and one specific cladding mode, Δn_{eff}, will change to ($\Delta n_{eff} + \delta(\Delta n_{eff})$) correspondingly. Consequently, a peak wavelength shift $\delta\lambda$ in the position of the m-order peak of each spatial frequency component originally at λ to a new position λ' could be observed in the interference spectrum. The peak wavelength shift $\delta\lambda$ can be expressed as follows:

$$\delta\lambda = \delta\left(\frac{\Delta n_{eff} L}{m}\right) = \left(\frac{\delta L}{L} + \frac{\delta(\Delta n_{eff})}{\Delta n_{eff}}\right)\lambda \tag{17}$$

and the associated phase shift $\delta\Phi$ is expressed as:

$$\delta\Phi = -\frac{2\pi(\Delta n_{eff}\delta L + L\delta(\Delta n_{eff}))}{\lambda} \tag{18}$$

2.2. Grating-Type Micro-Structured Fiber Optic Sensors

In grating structures, the forward and backward propagating modes are related with each other through [23]:

$$\vec{\beta}_b = \vec{\beta}_f + m\frac{2\pi}{\Lambda}\vec{j} \tag{19}$$

where m is the diffraction order, Λ is the period of the grating and j is the unit vector along fiber axis, $\beta_i = (2\pi/\lambda)n_{eff,i}$ ($i = f$ or b) is the propagation constant of forward or backward propagating modes. Equation (19) shows that the reciprocal vector provided by the periodical index modulation could compensate the momentum mismatch between the forward and backward propagating modes. The first-order diffraction in the microfiber-based FBGs is expressed as:

$$(n_{eff,f} + n_{eff,b})\Lambda = \lambda_B \tag{20}$$

where λ_B is the Bragg resonance wavelength. When the forward and backward modes are identical, the Bragg resonance condition will be met, namely $\lambda_B = 2n_{eff}\Lambda$.

The effective index and the period of the grating in the above function are tightly related to the radius of the microfiber, the RI of fiber, the surrounding RI, temperature, and strain, and could be described as follows for a microfiber-based FBG:

$$\lambda_B = 2n_{eff}(r, n, n_{ext}, T, \varepsilon)\Lambda(T, \varepsilon) \tag{21}$$

where r is the radius of the microfiber, n is the refractive index (RI) of silica, n_{ext} is the surrounding RI. When the external disturbances change any parameter in the above equation, the resonance wavelength would be shifted correspondingly, leading to the possibility of optical sensing.

3. Short Taper

Tapered optical fiber structures have attracted intense attentions over the past several decades and found a lot of applications such as power couplers, sensors, and add-drop multiplexers [24–27]. In general, fiber tapers could be categorized into two types: abrupt taper (non-adiabatic) and gradual taper (adiabatic). The main difference between the two types of fiber tapers lies in whether there is light energy in the core mode excited to the cladding modes through the tapered region which will be finally attenuated by the coating of the fiber. Hence, the gradual taper is usually fabricated by gradually tapering the optical fiber with small taper angles in order to minimize the insertion loss and normally refers to the adiabatic long taper. However, when the taper angle is large enough, i.e., the local taper length-scale is much smaller than the coupling length between the fundamental and higher-order cladding mode, that some energy in the core region will be coupled into the cladding region, the tapered structure forms an abrupt taper. Most of the short tapers refer to the abrupt tapers, which are commonly manufactured by electrical arc method using built-in fiber tapering programs in a fusion splicer. The up-taper and down-taper regions usually have steep slopes and the taper waist could be in the range of several microns to tens of microns controlled by the magnitude of the electric arc, stretching time and speed. Figure 1 gives a typical image profile of the abrupt taper.

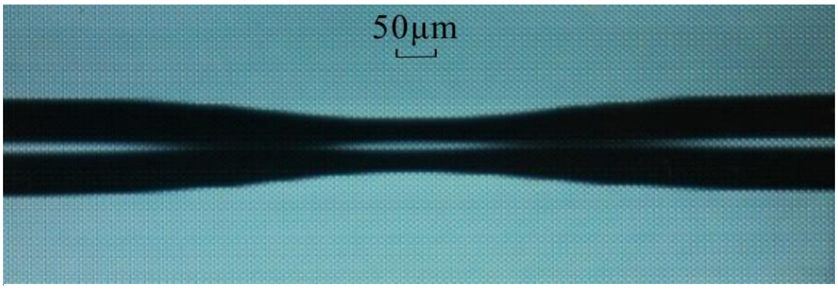

Figure 1. Image profile of an abrupt taper [11].

Recently, several new fabrication methods for short abrupt tapers have been proposed and demonstrated in experiments. For example, a high-frequency pulsed CO_2 laser with a maximum average output power of 10 W was employed to modify the fiber structure by applying a constant tension to the ends of the fiber [28]; in [29], a compact abrupt taper MI was manufactured by fusion splicing the fiber taper with two normal cleaved fiber ends; a more straightforward method was proposed in [30], where the abrupt taper was made by directly fusion splicing two normal cleaved fiber ends. These methods provide more access to the abrupt taper manufacturing and bring multiple configurations to the abrupt taper structure.

Fiber-optic sensors based on abrupt tapers are realized by concatenating two short abrupt tapers to form a MZI. The two tapers act as two light steering elements to couple light to high-order modes and back to the fundamental mode. When the input light passes through the first taper, part of the energy would be coupled into high-order modes because of the steep slope of the taper. In principle, the steeper the slope, the more energy will be coupled to high-order modes and a larger number of modes will be excited. At the second taper, high-order modes are coupled back to the fundamental mode and the output interference signal is a result of multi-mode coupling. It is noted that the two-taper structure enhances the interference fringes much more significantly than the single-taper structure and the coating along the SMF between the two tapers should be removed preventing the energy loss. The taper size determines the contrast and uniformity of the interference fringes, and the separation distance between the two tapers controls the free spectral range (FSR) of the output signal. The phase difference between the core mode and cladding modes could be approximated as:

$$\varphi = \frac{2\pi \Delta n_{eff} L}{\lambda} \tag{22}$$

where L is separation between the two tapers; Δn_{eff} is the effective RI difference between the core mode and cladding modes; λ is the input wavelength. Any disturbances on the length L and the effective RI difference will induce the variation in the phase. When a broadband light is used as the light source for the sensor, the output spectrum would be the interference spectrum induced by the tapered structures. The shift of the attenuation peaks could thus be utilized for monitoring the parameters that cause the change in the phase difference.

The two abrupt tapers-based MZI has been demonstrated with high sensitivities to various external disturbances, such as temperature, strain, refractive index, liquid level, lateral stress and so on. Single parameter measurement was pioneered in [31,32], where the RI and strain were quantified. The following works also achieved curvature [33], lateral stress [34], liquid level [35], and enhanced sensitivity for RI [36] measurements. The aforementioned measurements all employed the widely used peak wavelength shift method, which could be not practical when there is only small difference between the two spectra. To overcome this drawback, a novel spectrum differential integration (SDI) method was proposed and demonstrated as a more reliable method over a wide spectral range [37,38]. It has been proved that the SDI method can also be utilized with other kinds of modal interferometric sensors. To improve the contrast of the attenuation peaks and the sensing sensitivities, a novel double-pass two taper-based structure was proposed by connecting a gold-coated fiber mirror with the output end of the sensor [39]. The sensitivity was made nearly twice as large as those of the single-pass sensor. Recently a very interesting asymmetrical dual tapered fiber MZI was made in [40], where the two abrupt tapers have different tapered waists. It has been used for the directional tilt sensor.

In 2009, simultaneous dual-parameter measurement was successfully conducted using the two abrupt taper structures [41]. Temperature and RI could be simultaneously discriminated by utilizing S-band and C/L-band light sources. The resultant temperature and RI sensitivities are 23.188 nm/RIU (refractive index unit) and 0.071 nm/°C, and 26.087 nm/RIU and 0.077 nm/°C for different interference orders, which paves a way for multi-parameter sensing using the tapered structures. Temperature and liquid level discrimination was also realized in the later work [42].

A more compact and practical device was made by only one abrupt fiber taper with gold coating on the fiber end facet, forming an in-line MI. The only one fiber taper acts as the light steering elements exciting cladding modes as well as coupling cladding modes back to core mode. This novel, low-cost, and easy fabrication interferometer have found applications in RI sensing [43] and inclinometer sensor [44].

Making abrupt tapers in bend-insensitive fibers has brought a lot of unique features to the abrupt taper-based in-line MZI. As shown in Figure 2a, in the bend-insensitive fiber, the germanium-doped silica core is surrounded by a ring of nano-scale gas-filled voids, which divides the fiber cladding area into the inner and outer cladding regions. Inner cladding modes which are guided inside the inner cladding region and outer cladding modes that have energy distribution outside the inner cladding could be excited by the abrupt taper structure. Due to the different energy distribution of the inner cladding modes and outer cladding modes, the influences of the external disturbances on these modes are different. With appropriate adjustment of the specifications of the taper configuration, the excited inner and outer cladding modes could be selectively excited and employed for discrimination and measurements of multiple measurands. One of the significant works was the successful simultaneous measurements of temperature and RI in [45]. Figure 2b,c show the shifts in the transmission spectrum of the tapered bend-insensitive fiber interferometer with changes in ambient temperature and external RI. More parameters including temperature, axial strain, and RI were measured using the same structure in [46]. The guided and leaky modes in the tapered bend-insensitive fiber interferometer are further investigated in [47]. This work extends the operating range of the refractive index sensor into the regime of leaky outer cladding modes, which is previously inaccessible to similar sensors due to the complex nature of the phase dependence of the leaky modes on external refractive index. Besides the static parameter measurements using the tapered bend-insensitive fiber interferometer, dynamic measurements such as damped and continuous vibrations were also realized for the first time using this kind of interferometer [48]. With the unique double cladding structure of bend-insensitive fiber, it is possible to manufacture an abrupt taper-based MZI without removing its central protective jacket, which renders many great advantages in vibration sensing applications, such as maintaining high mechanical strength, allowing easy fiber attachment to a substrate, and isolating the optical fiber from external physical damage. Keeping the central protective jacket also enables large attenuation of the outer-cladding modes, which leaves only a few number of inner-cladding modes propagating along the bend-insensitive fiber and guarantees a more uniform spectral response for the dynamic sensing. Similar work using tapered Er/Yb codoped fiber interferometer has also been published in [49].

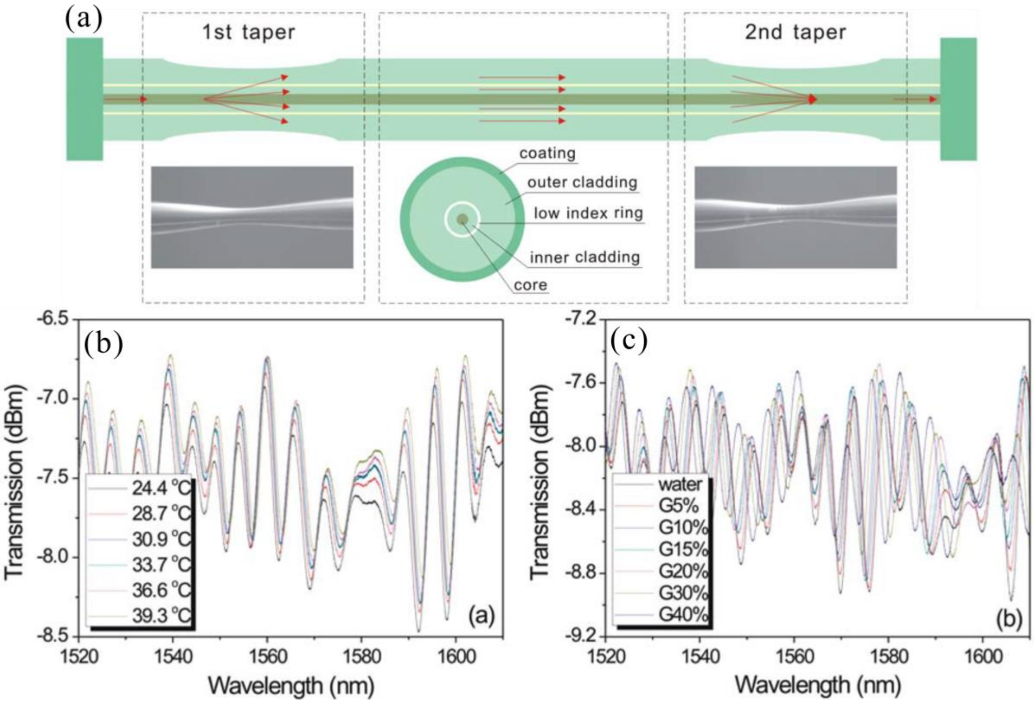

Figure 2. (**a**) Schematic illustration of the tapered bend-insensitive fiber interferometer; Shift in the transmission spectrum with a change in (**b**) ambient temperature and (**c**) external RI [45].

Novel short abrupt tapers have been proposed and fabricated with different taper configurations. Up-taper has a taper waist whose diameter is larger than the fiber diameter as shown in Figure 3a. The enlarged-waist tapers could also be used to excite cladding modes and couple them back to the fiber core. By concatenating two up-tapers along the fiber [50–59], the in-line MZI owns similar performance as the normal abrupt taper-based interferometer. Another type of abrupt taper is the S-taper, which is tapered by a fusion splicer with a non-axial pull as shown in Figure 3b. S-taper itself could form the interferometer with excitation and coupling of cladding modes through two bending regions along the tapering length, which has been studied and demonstrated with higher sensitivities than normal abrupt taper-based interferometer sensors [60–64]. Other novel abrupt taper-based interferometers include three cascaded normal abrupt tapers [65], tapered thin optical fibers [66], and tapered hollow fibers [67].

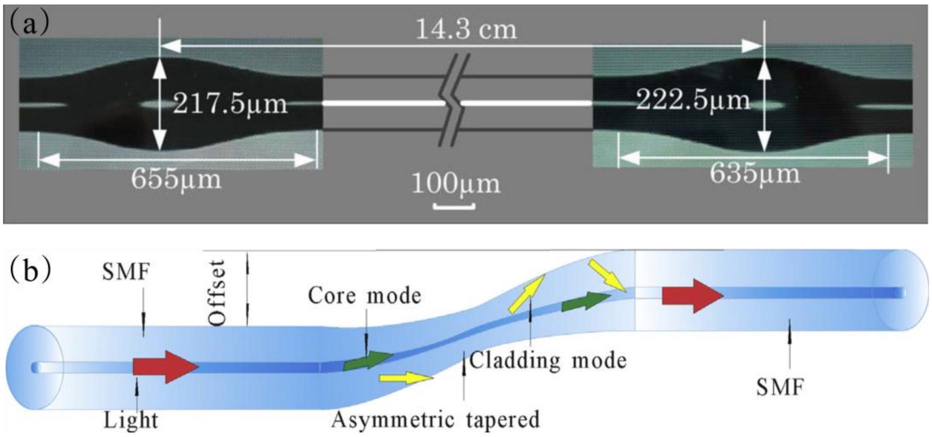

Figure 3. Schematic profiles of (**a**) Up-taper [54] and (**b**) S-taper [63].

4. Long Taper

4.1. Long Taper Profile and Fabrication Methods

Evanescent wave field decays significantly at the outer surface of the cladding of standard optical fibers, while with the introduction of low-loss tapered long fibers, evanescent wave could be guided along the extremely thin tapered waist section with considerable energy [68]. The partial overlap of the evanescent wave with the surrounding medium could be utilized for refractive index (RI) measurements, whose sensitivities are determined by the penetration depth and the intensity of the evanescent wave [69–71]. A typical schematic profile of the fiber long taper could be found in [72] and the microscope images of the taper waist and transition regions could be found in [73]. The fiber long taper usually consists of two parts: taper waist and taper transition regions. The long taper is firstly decreasing in diameter until a constant-diameter waist region is reached. Then it gradually increases back to the normal fiber diameter. The microscopic images show an example of the waist and transition regions of a typical long fiber taper.

The properties of the long fiber tapers could be easily controlled by adjusting the fabrication conditions. The slope or sharpness of the taper transition regions is a key factor that determines the taper features. Generally, long fiber taper could be divided into two categories depending on the slope of the taper angle [74]: adiabatic and non-adiabatic. An adiabatic taper is defined according to the adiabatic criterion as [72]:

$$\left|\frac{\mathrm{d}r}{\mathrm{d}z}\right| \leq \frac{r(\beta_1 - \beta_2)}{2\pi} \tag{23}$$

where β_1 and β_2 are respectively the local propagation constants, in the transition, of the fundamental mode and the higher order mode to which power is most likely to be lost; r is the radius of the adiabatic taper as a function of z, which is the distance along the taper longitudinal axis Usually an adiabatic taper has very small local change in the taper radius as shown in Figure 4a, leading to that the main portion of the light energy remains in the fundamental mode and does not transfer to higher-order modes. On the other hand, the non-adiabatic taper has a sharper taper angle as shown in Figure 4b and is capable of coupling the energy from the fundamental mode of the untapered fiber to the higher-order modes of the taper waveguide where more than one mode is supported. The effective refractive index difference induced by the surrounding material between these modes along the taper region would contribute to the phase difference between them and with the help of taper transition regions modal interference will occur and result in interfering spectral response.

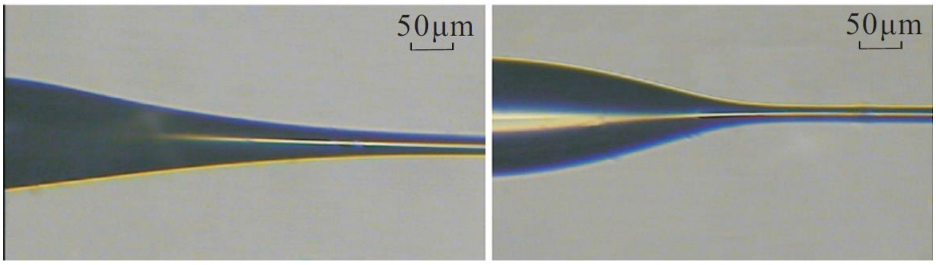

(**a**) (**b**)

Figure 4. The adiabatic taper (**a**) and non-adiabatic taper (**b**) [74].

A number of methods have been developed to fabricate the long fiber taper. A frequently used method is a heating and stretching technique [72,75,76]. As shown in Figure 5, a section of SMF is stretched by using two linear translation stages with submicron precision and its middle region is jacket-off. A small region of the fiber without jacket is heated by a hydrogen gas flame with millimeter dimension. The flame is scanned over a length of several centimeters along the fiber axis. After a pre-heating process, the fiber is elongated while the scanning range of the flame starts to increase.

The pulling speed of the translation stages, the scanning range of the flame, and the scanning speed are accurately controlled by the computer. Fiber tapers with gradual slopes in the down- and up-taper regions and long uniform waist region would thus be fabricated by the slow stretching technique. Other techniques including using a micro-furnace comprising a sapphire tube heated with CO_2 laser [77] and a designed electric strip heater [78] have been proposed to make low-loss tapers. In 2010, Zhang et al. [79] presented an etch method based on surface tension driven flows of hydrofluoric acid micro-droplets. Low-loss (less than 0.1 dB/mm), subwavelength-diameter long tapers could be successfully fabricated.

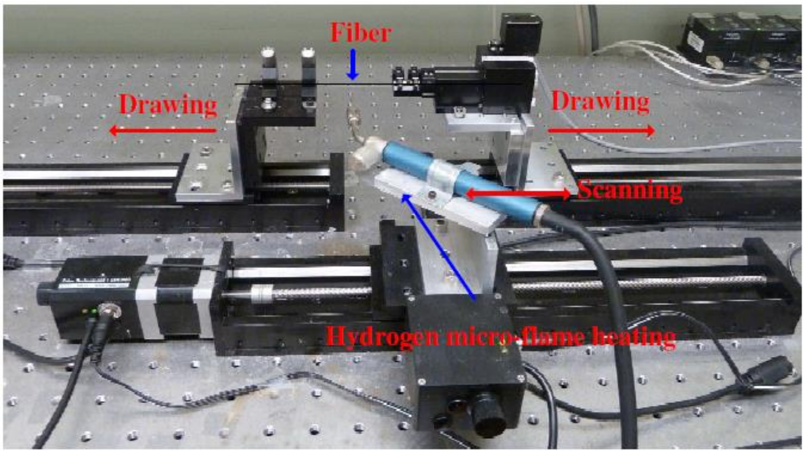

Figure 5. Experimental setup for H_2 flame heating and stretching technique [76].

4.2. Adiabatic Long Taper

A fiber long taper is adiabatic if the local taper angle is small enough so that there is no light energy transfer between different modes when the light propagates along the long taper [21,24]. In principle, the difference of effective refractive indices between LP_{01} and LP_{0m} modes determines the core taper adiabatic angle. If the core taper angle is greater than the adiabatic taper angle, energy from the fundamental mode will be coupled to the higher-order modes, making the long taper non-adiabatic.

Adiabatic long tapers have been used for all-fiber mode converters [80] and multiplexers [81]. It is also capable of coupling light in and out of other sensing structures for bio-chemical sensing such as liquid-core optical ring-resonators [82], micro-disks [83], and microspheres [84]. Also, the adiabatic tapered fiber has been used for the fabrication of the high sensitive surface plasmon resonance (SPR) sensor for the refractive index measurement. When the real part of the thin-film permittivity is negative and higher in magnitude than both its own imaginary part and the permittivity of the material surrounding the thin-film, the SPR phenomenon happens. In this case the coupling happens between the light propagating through the long taper and a surface plasmon [85]. Different materials have been coated along the taper surface to form surface plasmon sensors for temperature, refractive index and bio-sensing measurements [86–90]. Low-loss solgel-derived silica films were also successfully deposited on the uniform waist of a tapered fiber [91], which has the ability to dope with rare earths and other materials, leading to a new class of all-fiber devices for sensing applications. Recently, a simple noncontact displacement microfiber sensor [92] was proposed using an adiabatic long taper by bending it in a U-shape. The sensor is capable of measuring a wide displacement distance up to 12 mm with a sensitivity of 0.2 dB/mm at a minimum tapered diameter of 8 μm.

4.3. Non-Adiabatic Long Taper

Due to the relatively sharp taper angle, the fundamental mode originally transmitting through the normal optical fiber would transfer part of its energy to the cladding modes in the downtaper region [93]. Hence there would be more than one mode propagating along the taper waist. In the uptaper region, all modes are coupled back with each other, resulting in interference patterns. In this case, the non-adiabatic long taper behaves as a modal interferometer with a transmission given by:

$$I = I_1 + I_2 + 2\sqrt{I_1 I_2}\cos(\Delta\varphi) \tag{24}$$

where I is the intensity of the interference signal, I_1 and I_2 are the intensities of the lights propagating in the fundamental mode and higher-order mode respectively. $\Delta\phi$ is the phase difference between the interfering modes, which is approximately equal to:

$$\Delta\varphi = \frac{2\pi\Delta n_{eff} L}{\lambda} \tag{25}$$

where λ is the central wavelength of the light source; L is the length of the taper waist over which the fundamental mode and the cladding modes exist; Δn_{eff} is the effective refractive index difference between the modes. Any variations in the length L and the effective refractive index difference would force the phase difference to change, resulting in the shift of the output interference spectrum. For example if the temperature of the surrounding environment of the microfiber changes, the difference in propagation constants and the relative phase between different modes will be modified, leading to a shift in the spectral response.

It has been shown that mode coupling in non-adiabatic fiber tapers can be controlled to occur primarily between the fundamental core mode of the normal fiber and the first two modes of the taper waveguide (HE_{11} and HE_{12}), where the light propagates at the air-cladding interface of the taper's waist region. Consequently, the intensity and the penetration depth of the evanescent wave fields are significantly strengthened, leading to a larger overlap with the surrounding medium. The surrounding medium will make a different in the effective refractive index of the higher-order mode in the taper waveguide and change the value of Δn_{eff}. Thus, the spectra will respond with wavelength shift, which provides the parameter being monitored for the RI measurements.

RI measurement is one of the most popular sensing applications using the non-adiabatic long taper. The sensors are commonly based on standard single mode fibers (SMF) [94,95]. By tapering the diameter of an SMF to less than 1.64 μm, the fundamental core mode is no longer confined and converted to the fundamental cladding mode along the waist region, interfering with the first order cladding mode. This device achieves a high sensitivity of 980 nm/RIU for a RI range from 1.332 to 1.392 [96]. Later, a non-adiabatic long taper with ultrashort waist length of only 2.4 mm was proposed to increase the FSR up to 80 nm and achieved a maximum sensitivity of 25,667 nm/RIU for RI measurement [97]. In 2004, the non-adiabatic long taper was used for protein sensing, realizing a sensitivity of 1500 nm/RIU for RI measurement and 2.42141 nm/%W/V for protein concentration detection [73]. Displacement and temperature measurements were also realized using the long taper with sensitivities of 4.2 pm/μm and 12.1 pm/°C, respectively [98]. Another important application is the magnetic field measurement, which has been conducted by inserting the long taper into the magnetic fluid [99–101]. The RI of the magnetic fluid could be measured for the quantification of the magnetic field. Hydrogen sensing was also available using the long taper by employing the strong evanescent field interaction with the Palladium overlay. A spectral shift of −1.99 nm with the injecting hydrogen of a concentration of 5% was observed using a long taper with waist diameter of 3 μm [102].

Despite the static measurand quantification, our group has proposed for the first time the acoustic vibration detection using the long taper [103] as shown in Figure 6a. The long taper acted as the sensing arm in the conventional dual-arm MZI formed by a combination with a reference arm. With a thin waist diameter of 1.7 μm, the proposed sensor has a 20 dB improvement in the signal to noise ratio and is comparable with the performance of the commercial piezoelectric accelerometer as shown in Figure 6b. A unique taper-based RI sensor at the air/solution interface was also studied in our group [104], which reveals an interesting phenomenon that the visibility of the spectral interference of the sensor at the air/solution interface is significantly reduced. This is because the coupling between the fundamental cladding mode and higher-order asymmetric cladding modes is very weak and extremely sensitive to the external RI. Other novel ideas include the high-sensitivity force measurement by long taper with the help of the Optical Frequency Domain Reflectometry (OFDR) system [105] and tapered polarization maintaining (PM) fiber for the current sensing [106]. These works systematically characterized the fundamental properties of the long taper in terms of the possible higher-order asymmetric cladding modes, evolution of the state of polarization of the light along the taper and so on, which definitely deepens the understanding of the underlying physics of the non-adiabatic taper.

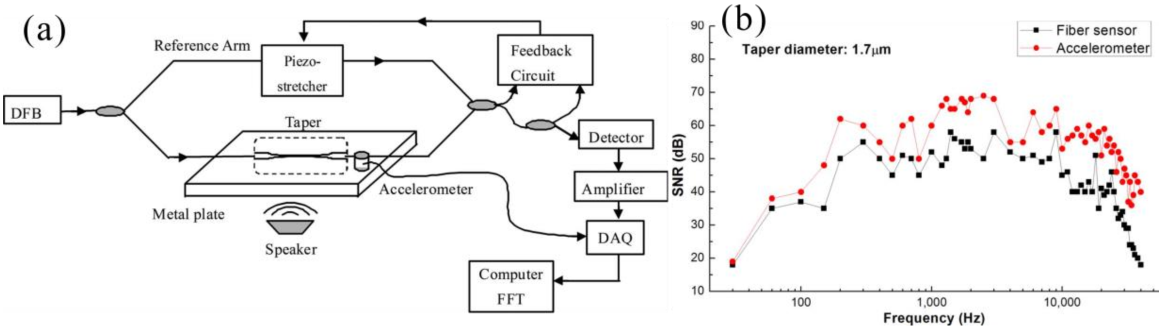

Figure 6. (**a**) Schematic of experimental setup; (**b**) Frequency responses of the taper sensor and piezoelectric accelerometer [103].

4.4. Non-Adiabatic Long Taper Based on Different Optical Fibers

Non-adiabatic long tapers have also been made using different kinds of optical fibers in order to diversify the applications. Multimode fiber (MMF) is one of the examples. Tapered MMF was firstly proposed in 1984 by Kumar et al. to measure RI with a high degree of accuracy [107]. In 2004, Villiatoro et al. [108] presented a new fiber optic RI sensor based on the radiation losses induced by the sample medium in the tapered region of a MMF. It was demonstrated that the sensor was able to measure the RI in the range of 1.36–1.46, as well as RI changes below 10^{-4}. Later in 2011, a novel fiber refractometer with enhanced evanescent field was fabricated based on a tapered MMF sandwiched between two SMFs [109]. With large overlap between the evanescent wave and the surrounding medium, the RI sensitivity was achieved with better than 1900 nm/RIU at a RI of 1.44. The RI sensitivity was further improved to 2946 nm/RIU in [110] with a similar configuration. In 2014, a tapered MMF-based dual MZI is proposed and demonstrated for simultaneous measurement of RI and temperature [111]. Two groups of interferences including the interference between the fundamental mode and the high-order mode of the tapered MMF, as well as the interference between the high-order mode of the tapered MMF and the reference arm were realized for sensing applications.

The photonic crystal fiber (PCF) with the photonic bandgap structure has properties that make them useful for the next generation photonic device applications. Wavelengths that lie within the bandgap would not be allowed to transmit through the PCF, leading to the applications of the filtering and confinement of PCF [112]. Tapering PCF has promised a great potential in further expanding the capability of optical fibers. To date, tapered PCFs have been made for mode conversion and to further engineer the dispersion and non-linearity along the fiber. They have been also used for lowering the threshold for supercontinuum generation and dispersion management [113]. The process of tapering PCF is accompanied with the collapsing of the air holes, which transforms a zone of the PCF into a solid unclad multimode optical fiber [114,115]. Consequently, the fundamental mode HE_{11} in the PCF is coupled to the higher-order guided modes HE_{1m} of the tapered fiber. The oscillatory pattern could be obtained with the interference between these guided modes, thus providing the opportunities for sensing applications [116,117]. Earlier sensing works including RI, strain, and temperature measurements using tapered PCF were conducted by Villiatoro et al. in 2006 [114,115,118,119]. Recent developments on this topic involve employing an acid micro-droplets etching method for tapering the PCF [120], where a more uniformly and thinly tapered PCF was realized with a 100 times improvement in the sensitivity for RI measurement. Temperature-independent curvature [121] and RI [122] measurements using tapered PCF were realized in 2012 with sensitivities of up to 8.35 dB/m^{-1} and 1529 nm/RIU, respectively. In the same year, a slightly tapered and elongated PCF was fabricated to achieve an ultrahigh RI sensitivity of more than 1600 nm/RIU [123]. A novel and compact magnetic field sensor was achieved by a tapered PCF coated with ferrofluid [124]. The sensor had a sensitivity of 16.04 pm/Gs and resolution of 0.62 Gs in the experiments.

Small core single-mode fiber (SCSMF) has also been used for forming a long taper interferometer. The SCSMF has a small core diameter of 2.2 µm [125] and was sandwiched between two standard SMFs. The tapering process was performed using the microheater brushing technique [126]. It is demonstrated that the fiber sensor with a waist diameter of 12.5 µm shows the best sensitivity of 19,212.5 nm/RIU in the RI range of 1.4304–1.4320. Furthermore, the relative humidity (RH) was successfully measured by the sensor without any coating materials and a maximum sensitivity of 18.3 nm per RH unit (RHU) was achieved in the RH range of 90.4%–94.5% RH.

5. Resonator-Type Microstructures

Resonator-type microstructures have been intensively investigated and studied recently in a wide variety of applications including optical filters, sensors and lasers due to the unique low-loss and high quality factor (Q) features [127]. The working principle of the resonator-type microstructures relies on the overlapping and coupling of the evanescent waves of the modes propagating in adjacent turns by coiling the microfiber onto itself. The Q factor of this kind of resonators can go beyond 100,000 in loop and coil structures [128,129]. Typical resonator-type microstructures are categorized into three types: loop, knot, and multi-coil [127].

5.1. Microfiber Loops

The microfiber loop structure is the simplest one among the resonator-type microstructures, which is fabricated by manufacturing the microfiber and bending it into a self-coupling loop [130]. The first loop resonator was demonstrated in 1989 by Caspar et al. [131]. The effect of birefringence, the shape of resonances, and the free spectrum range that determines the spectral characteristics could be adjusted by the alignment of the input and output ends of the loop to vary the microfiber self-coupling, which were attached to each other through the Vander Waals and electrostatic forces [132]. However, this configuration is fragile, especially in liquid environment due to the electrostatic forces. In order to enhance the physical robustness of the microfiber loop for applications in liquid, the loop resonator was constructed by wrapping the microfiber around a 460 µm diameter copper rod as shown in Figure 7a [133]. With the support of copper-rod, the microfiber loop exhibits high stability and flexibility and achieves critical coupling within a broad spectral range [134], enabling high-sensitivity optical sensing in both low- and high-concentration solutions (Figure 7b,c).

Although the rod-supported microfiber loop has been proved to be an effective way to tackle the sensor stability issue, there are still some problems presented by this technique such as additional loss induced by the rod, preventing the access to the surface of the device as so on. To overcome these drawbacks, a novel methodology has been adopted to fuse the coupling region of the microfiber loop by using a CO_2 laser [135]. A 3-mm-wide CO_2 laser beam was focused to a spot size of 800 m onto the region where the microfiber looped over itself at a power of 5 W for a duration of 30 s. This resulted in the overlapped microfiber segments fusing onto each other laterally. The CO_2 fusing method not only improves the robustness of the device, but also enables coupling in cases where the evanescent waves are weak. An improved scheme was proposed by Wang et al. in 2010 to make a free-standing microfiber closed-loop resonator by fusing two ends of a piece of microfiber [136]. The resonator was able to be tuned and had an extremely high W-factor of 110,500 with a finesse of 15.3.

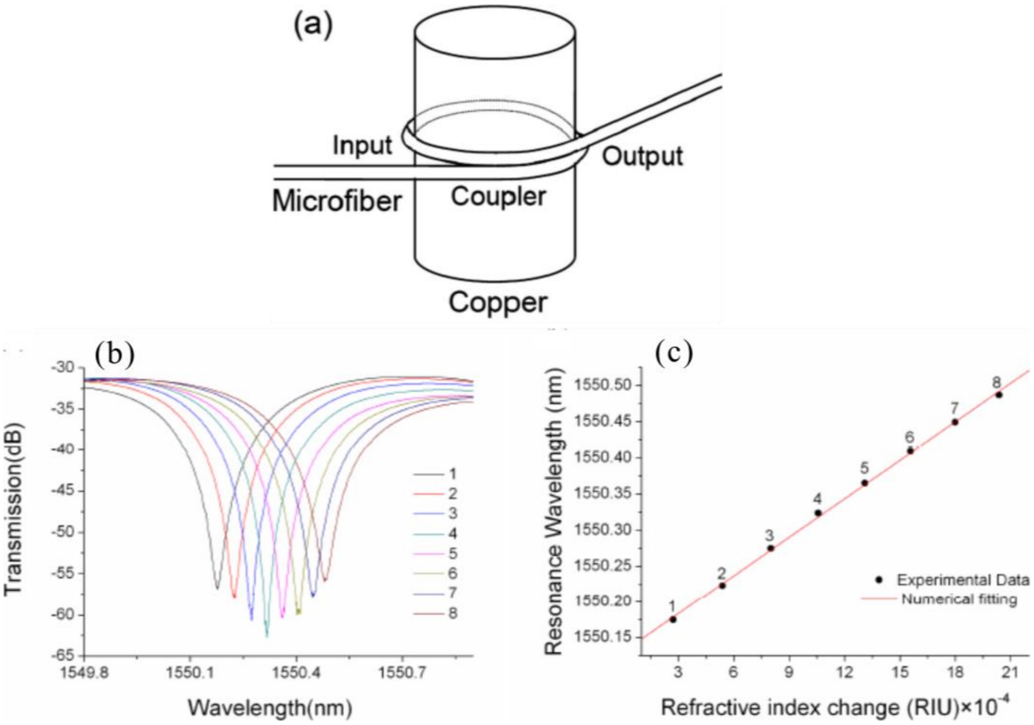

Figure 7. (**a**) Schematic side view of a copper rod supported microfiber loop [133]; (**b**) Spectral shifts of a resonant peak caused by index change of the solution; and (**c**) resonant wavelength as a function of the RI change [134].

Recent studies on microfiber loops have focused on their sensing applications. The resonant and waveguide properties of microfiber loop were investigated for RI and salinity sensing of seawater [137]. It is shown that the sensitivity of the loop resonator increases with the increase of wavelength and the decrease of diameter of the loop. In 2013, the microfiber loop was placed inside a sealed Poly(methyl methacrylate) (PMMA) chamber to measure the RH [138]. As the effective RI of the evanescent wave in the microfiber is modified by environmental humidity, the resonant wavelength of the resonator changes with RH level. In 2015, a highly sensitive current sensor was proposed and experimentally demonstrated based on an optical microfiber loop resonator (MLR) incorporating low index polymer [139]. The microfiber was wrapped around the nichrome wire with low index polymer overlay, which is able to reduce the round-trip loss and improve the Q-factor and finesse of the MLR.

5.2. Microfiber Knots

Instead of employing the Vander Waals or electrostatic forces in the microfiber loop case, a knot structure was made to increase the robustness and flexibility of the microfiber devices [140,141]. The first microfiber knot structure was reported by Tong et al. in 2003 as shown in Figure 8a [142], where a 950 nm diameter microfiber was coiled to a 150 µm diameter knot with a Q factor of 1500 around 1.5 µm wavelength. In 2006, a microfiber knot with improved Q factor of 57,000 with finesse of 22 was fabricated as shown in Figure 8b [143]. The knot resonator was highly stable in water with Q factor up to 31,000 and finesse of 13. A solid MgF_2 substrate was also used to support the knot structure. In 2007, Vienne et al. embedded the MNF knot structures in low refractive index polymer, and investigated the effect of host polymer on the resonators [144]. Later, a robust and compact microfiber knot assembled by two fiber probes was placed on a plate glass substrate and coated with low-index polymer for temperature sensing [145]. Sensitivity of the sensor was achieved with 0.27 nm/°C. A polymer fiber-based micro-knot has also been investigated by Rao et al. as temperature and humidity sensors [146,147]. The work was conducted by comparing the sensing performance of polymer fiber-based micro-knot with regular SMF-based micro-knot. The polymer fiber-based micro-knot has a higher temperature sensitivity of 266 pm/°C than that of the SMF-based micro-knot, but limited temperature sensing range. Figure 9a shows the Scanning Electron Microscope (SEM) images of the SMF/polymer fiber-based micro-knots. Figure 9b,c shows the compact sensor made from the micro-knots and the experimental setup for the humidity sensing. The thermal properties of the microfiber knot were further investigated in [148]. Current sensor was also realized by wrapping the microfiber knot around the copper wire which has electric current transmitting through it [149]. The resonant wavelength shift was due to the thermally induced optical phase shift, which was owing to the heat produced by the flow of current in the copper wire. Magnetic field was also measured by immersing the microfiber knot into the magnetic fluid [150]. In order to avoid the evanescent energy leaking into the substrate with higher RI, the microfiber knot was partially embedded in the polymer layer. RI of surrounding solutions has also been measured by the microfiber knot in several works [151–153].

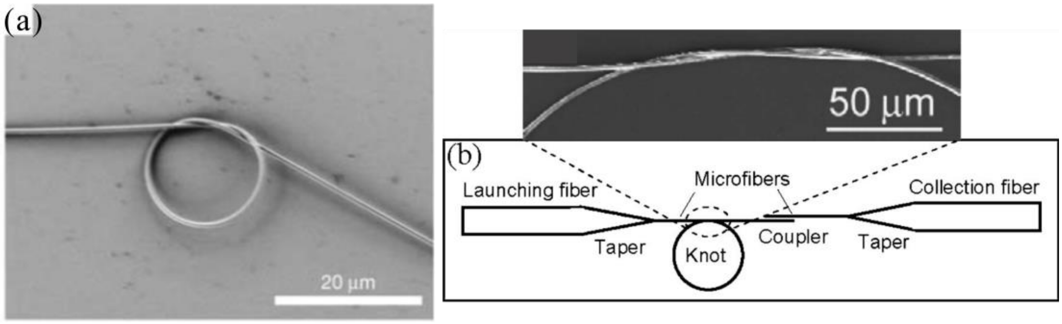

Figure 8. (**a**) Scanning Electron Microscope (SEM) image of a 15 μm diameter microfiber knot [142]; (**b**) SEM image and schematic of a 2.66 μm diameter knot [143].

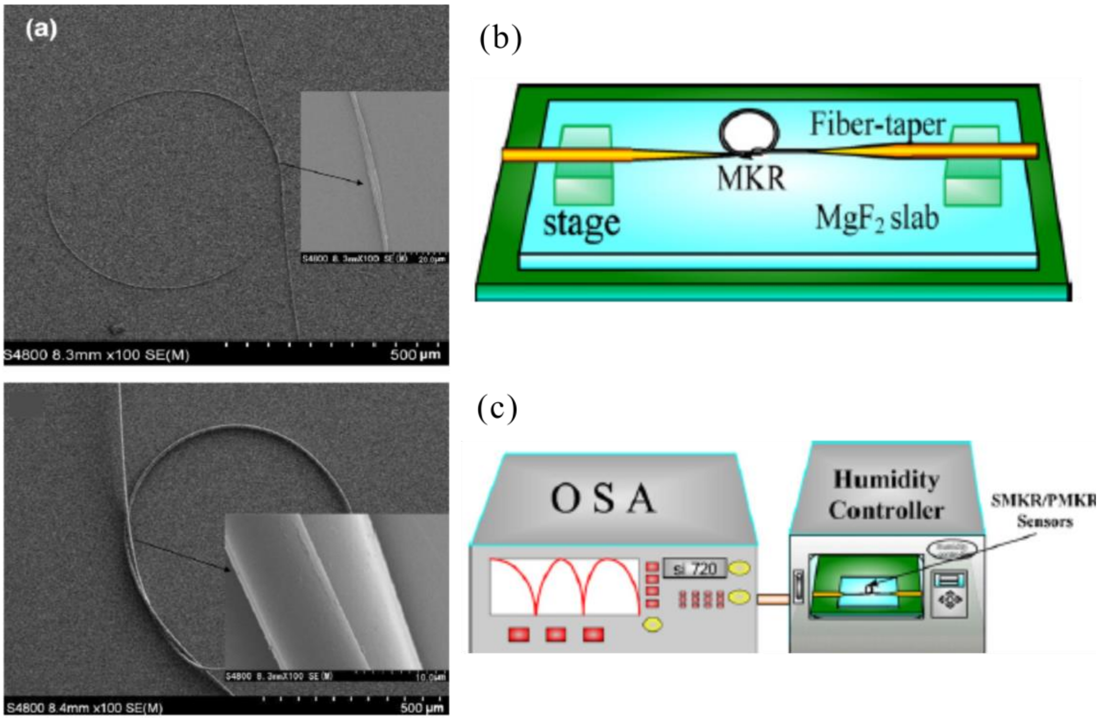

Figure 9. (**a**) SEM image of the single mode fibers (SMF)/polymer fiber-based micro-knots; (**b**) Sensing structure of micro-knot sensor; (**c**) experimental setup for humidity sensing [147].

Recently, our group proposed a novel phase-shift detection scheme in a FFT-based spectrum analysis technique for temperature sensing using the microfiber knot [154]. The microfiber knot was made with a ring diameter of 273 µm and the diameter of the microfiber was 6.75 µm as shown in Figure 10a. Optical modes experiencing completed different amounts of round-trips within the ring structure lead to multiple transmission peaks in the FFT spectrum of the device. Experimental results show that different peaks have distinct temperature sensitivities with values up to −0.542 rad/°C as shown in Figure 10b, which is about 10 times greater than that of a regular adiabatic taper MZI when using similar phase-demodulation schemes.

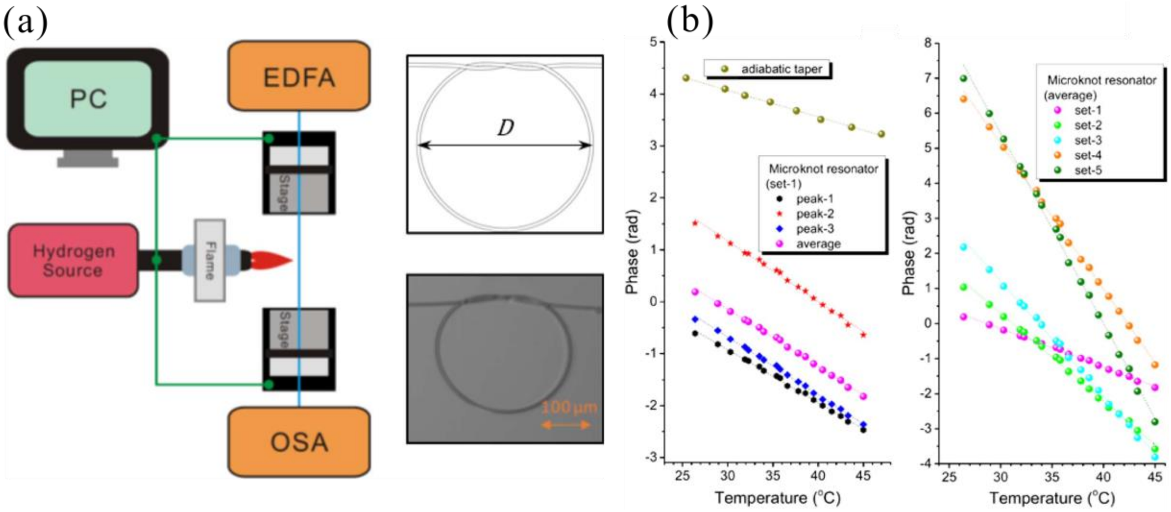

Figure 10. (**a**) Microscopic image of the microfiber knot and schematic setup of the temperature sensor; (**b**) Phase shifts of the fast Fourier transform (FFT) spectrum peaks as a function of temperature [154].

Other kinds of microfiber knot-based structures include a hybrid structure consisting of a microfiber knot resonator and a microfiber MZI [155], a miniature polarimetric interferometer by twisting a highly-birefringent microfiber [156], microfiber double-knot resonator [157], cascaded microfiber knot resonator [158], microfiber knot fused by CO_2 laser [159].

5.3. Microfiber Coils

The microfiber coil resonator is a 3D resonator with self-coupled adjacent loops in a helix arrangement. It can be easily made by wrapping a microfiber around a low-index rod in several coils [160,161]. The first theoretical investigation of the microfiber coil resonator could be found in [162]. It is shown that the light confinement in a coil resonator is achieved by appropriate self-coupling between turns and it has a one-dimensional structure of resonances. Different types of fundamental profiles of the microfiber coil resonators such as uniform, conical, and biconical have been theoretically studied [163]. Results suggested that ultra-high-Q resonators can be successfully fabricated when the micro-coil resonator has a biconical profile. Other theoretical works including a mathematical model that exemplifies the manufacture of the microfiber coil resonator with rotational and translational stages controlled by a computer [164] and dispersion studies revealing that the adjacent ring coupling in the microfiber coil resonator has notable contribution to the total dispersion [165] have been performed.

The first experimentally realized microfiber coil resonator was made in 2007 [166], where two-turn, three-turn, and four-turn coils were fabricated by wrapping the microfiber on a low-index rod. Also, the microfiber coil was coated with a Teflon resin, which has an extremely low refractive index (n~1.3 at 1.55 µm wavelength) and provides a uniform refractive index surrounding to the microfiber [167]. The fabricated resonator obtained an extinction ratio of 10 dB and free spectrum range of 1 nm, which has been used for RI measurement in the following works [168,169]. In 2009, the effect of rotation on the propagation of electromagnetic waves in optical micro-coil resonator structures was studied by Scheuer [170]. It is shown that an enhancement of orders of magnitudes of the Sagnac phase shift could be realized by the combination of slow-light and conventional propagation mechanisms, which can be used for the realization of highly compact optical rotation sensors and gyroscopes. Later, similar structure was made by coating the coil resonator with Teflon and wrapping around a PMMA rod which was then resolved in acetone, leaving a microchannel that could be filled by analyte [171]. In order to enhance the quality factor of the coil resonator, the coil number was increased in [172]. A high Q factor of 470,000 was achieved. A unique acoustic sensor was demonstrated in 2012 by coiling a microfiber around a 3mm diameter air-backed mandrel [173]. Local pressure variations were induced by acoustic waves and changed the mandrel diameter and thus the optical path length of the mode propagating in the microfiber. Temperature measurement was also conducted by wrapping a microfiber around a Teflon tube [174]. The probe is able to slide along electrical wires to map the local temperature for locating insulation faults and reporting high current surges. A temperature sensitivity of 95 pm/°C up to 80 °C was demonstrated. This sensor is cost-effective and simple to fabricate, making it attractive for industrial applications. A current sensor was proposed in 2014 by coiling the microfiber around a Chrome-nickel wire which is conductive to current [175]. The obtained current sensitivity was as high as 220.65 nm/A^2, which was two orders of magnitude higher than the previous results.

Recently, graphene-microfiber-integrated coil resonator has attracted intense interest for the unique properties of graphene [176,177]. Graphene is the most promising candidate for future high-speed electronic applications due to high carrier mobility and large saturation velocity. Chemical vapor deposition (CVD) techniques have been applied to grow high quality monolayer graphene sheet on the metal substrate, such as Cu, Pt, and Ir. monolayer graphene has a large sheet resistance and is perfect for fiber-optic-based electrical current sensors based on thermal effect. Metal films can provide a large sheet resistance, which is also applicable to the sensor. A thin layer of low-index Teflon was initially coated on the rod surface to prevent the loss induced by its relatively high-index. A monolayer graphene sheet grown by CVD was then mechanically transferred onto the surface of the Teflon coating as shown in Figure 11. The resonant wavelength will be shifted by the heat generated from electrical current due to the thermal effect in the microfiber resonator. The sensor exhibits a high sensitivity of 67.297 μm/A^2, which is two orders of magnitude higher than that reported earlier.

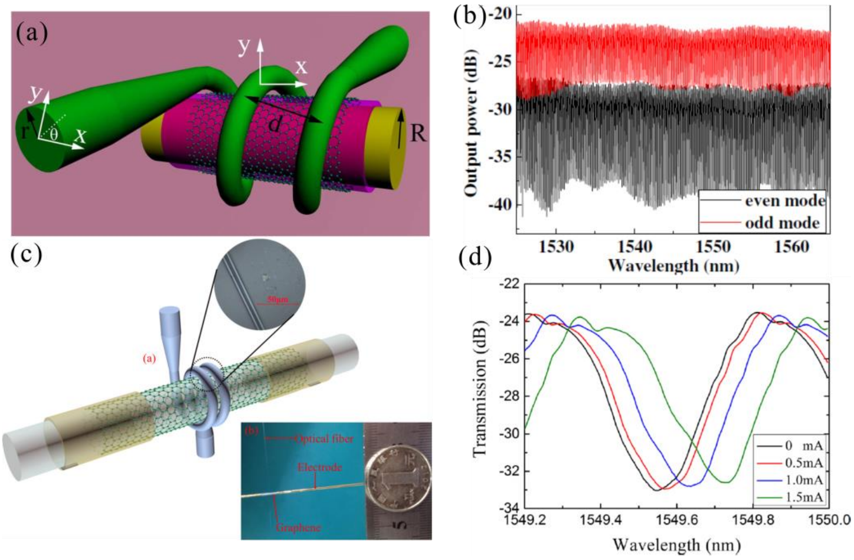

Figure 11. (**a**) Schematic of a graphene-based microfiber coil resonator as an in-line polarizer; (**b**) its transmission spectra for two orthogonal modes [176]; (**c**) The schematic diagram of the graphene-based electrical current sensor; and (**d**) its transmission spectrum shifts with different electric currents [177].

6. Micro-Machined Devices

Miniaturizing the fiber-optic point sensors has been highly demanded continuously for applications in tiny spaces. New functional in-line miniature sensors have been demonstrated as excellent candidates for high temperature and strain and pressure measurements [14]. For the purpose of easy-fabrication and mass production, several novel fabrication techniques have been proposed including laser micro-machining, chemical etching, focused ion beam method and so on. These new techniques pave the way for developing highly compact sensing devices, which largely enrich the family of fiber-optic point sensors.

6.1. Laser Micro-Machined Devices

With the advancements of laser technology, new fabrication methods for micro-structured fiber-optic sensors have been employed [178]. In particular, femtosecond laser and excimer laser are good candidates due to their high instantaneous power and high single-photon energy, which is able to ablate the micro-structure with good quality [179,180].

When the femtosecond laser is focused onto the optical fiber, the energy absorption occurs through nonlinear phenomena including multi-photon absorption, tunneling, and avalanche ionization. The influence of femtosecond laser modification upon the material can be divided into destructive and nondestructive according to the power magnitude utilized. Nondestructive fabrication means the power of the laser is below the ablation threshold of the material and the modification result shows a changed refractive index profile of the material by the laser source. This effect has found applications in optical waveguides, gratings, and directional couplers [181–183], etc. In contrast, the destructive fabrication uses a power higher than the ablation threshold of the target material, which can directly sculpture the material into desired structures. Here we focus on the destructive effects of the femtosecond laser on optical fibers and the resultant micro-machined devices.

Depending on different laser modification configurations, the micro-machined devices could be divided into two categories: the MZI and FPI.

One typical example of the MZI type micro-machined devices is demonstrated in 2010 [184]. The micro-cavity was fabricated by the femtosecond pulse ablation with a scanning speed of 20 μm/s along the fiber length. The transmission spectra of the device were monitored during the manufacturing. The scanning cycle was finished until the largest fringe visibility was obtained. Then the micro-cavity created with a cavity length of 85 μm was cleaned with methanol. As only part of the fiber core was ablated, light would be split into two paths with one transmitting through the cavity and the other through the remaining core. The difference of the effective refractive index between the core and the cavity induced the phase difference and lead to the formation of MZI. The sensor is used to achieve a high temperature measurement with a sensitivity of 0.046 nm/°C.

Another MZI type device was made in a different configuration. The femtosecond laser is used to fabricate a micro-hole in the center of a fiber end [185]. Then a micro-air-cavity is formed by splicing the micro-structured fiber end with a normal fiber end. Two micro-air-cavities were fabricated in the senor and act as light steering elements to excite and couple back cladding modes. The interferometer is applied for high-temperature sensing in the range of 500–1200 °C with a sensitivity of 109 pm/°C. An interesting configuration consisting of a trench embedded in a fiber taper was proposed in 2014 [186]. The fiber taper was fabricated on SMF by using a fusion splicer and the trench was written into the taper region by employing femtosecond (fs) ablation. The trench was able to excite the cladding modes from the core mode and the taper end coupled all the lights back. The sensor was successfully applied for gas RI measurement with sensitivity of 669.502 nm/RIU.

The most commonly seen devices made from the fs modification are the FPI type. In 2007, Rao et al. proposed for the first time directly machining a micro FPI on a SMF and a PCF using near-infrared femtosecond (fs) laser [187]. In the fabrication process, the focused spot size of the fs laser was 5 μm and the pulse energy was 20 μJ. A single pass exposure over an area of 80 μm × 30 μm was carried out on the SMF and PCF. This process was repeated several times until the designed ablated Fabry-Perot (FP) cavity was formed. The cavity was made across the whole fiber core so as all light energy will transmit through the cavity without any in the fiber core. Due to the low reflectivity of the laser-ablated surface, multiple reflections could be neglected for the contribution to the FPI interference spectrum. Thus, the low finesse FPI could be modeled using the following equation [188]:

$$I = I_1 + I_2 + 2\sqrt{I_1 I_2}\cos(\frac{4\pi nL}{\lambda} + \phi_0) \tag{26}$$

where I is the intensity of the interference signal; I_1 and I_2 are the reflections at the two cavity endfaces, respectively; ϕ_0 is the initial phase of the FPI; L is the cavity length, n is the RI of the medium inside the cavity, lambda is the optical wavelength. Thus, any change in the cavity length or RI of the medium inside the cavity will cause the interference fringes to shift. Temperature and strain response of the senor were also characterized in that work. However, the fringe visibility of the micro-structure device was only 2 dB, which was soon improved by the following works conducted by Xiao et al. [188,189]. In [189], a similar method was employed to fabricate a micro-notch in a SMF. The device had a loss of 16 dB but a significantly improved interference visibility exceeding 14 dB. It was tested to survive in harsh environment with high temperature up to 1100 °C. In 2009, the fs laser fabricated device was applied to the RI measurements by directly immersing into the RI liquid samples [190]. Thus, the micro-cavity was filled with solutions with different concentrations, leading to the change in the phase difference of the formed FPI. The highest resolution of 6.7×10^{-5} was obtained in the RI range of 1.37–1.42. Another RI sensor based on the fs laser modification is realized with the combination of fusion splicing [191]. Firstly, a micro-hole was inscribed by the fs laser at the cleaved fiber end facet. Then the modified cleaved fiber end was fusion spliced with a normal SMF to form a hollow sphere. By filling in the micro-cavity with RI solutions, the measurement sensitivity obtained was 994 nm/RIU. Another single micro-channel high temperature fiber sensor was achieved by drilling a micro-channel across the fiber core near the end of the common SMF using the fs laser-induced water breakdown [192]. The sensor has a good performance as a high temperature sensor up to 1000 °C.

The excimer laser is a kind of ultraviolet laser which is commonly used in the production of microelectronic devices, semiconductor-based integrated circuits or chips, and micromachining. The F_2 laser is one of them, producing 7.9 eV photons that are known to damage ultraviolet-grade fused silica glasses in long exposures. In Germania-doped glasses, the 157 nm photons emitted by the excimer laser directly bridge the 7.1 eV bandgap, allowing access to strong single-photon photosensitivity mechanisms without the need of traditional enhancement techniques.

A typical work using the excimer laser to micro-machine the optical fiber was shown in [193]. Fiber silica has an optical absorption coefficient of ~20,000 cm^{-1} at 157 nm, which forms the base to achieve high-quality micro-machining on fibers. Around 1600 laser pulses were used to complete the fabrication of the FPI in the PCF. The sensor has an excellent fringe visibility of 26 dB and acted as an ideal sensor for precise strain and high temperature measurement. The following work also used the excimer laser to make a micro-FPI near the far end of the SMF as a sensing tip [194]. Such a compact sensor could provide temperature-independent measurement of any RI larger than that of air with an RI resolution of 4×10^{-5}. Two miniature all-fiber in-line tip pressure sensors were also fabricated by the excimer laser, one with reflective coating and the other without coating [195]. But they showed similar pressure sensitivity of 0.01 rad/MPa and a temperature dependence of 0.05 mrad/K. Later, cascaded micro-FP cavities were fabricated by the excimer laser for simultaneous measurement of high temperature and RI [196]. The sensor head consists of a short air extrinsic FP cavity and an intrinsic SMF FP cavity, which have difference dependences on temperature, strain, and RI.

6.2. Chemically Etched Devices

Chemical etching has provided another alternative method for making micro-machined fiber architectures. The advantages of chemical etching include reproducibility, reliability, surface smoothness, and good symmetry. Various etching methods such as hydrofluoric (HF) acid static etching, HF acid dynamic etching, and tube etching have been proposed to date. The etched fiber shapes generally include the fiber tip and fiber micro-hole structures.

A typical fiber tip structure using the chemical etching method is proposed in [197]. The fiber tip was produced by firstly removing the fiber jacket and immersing the fiber in a melting polymer to form a protective layer with a tapered shape. Then the fiber was etched by 40% (v/v) HF solution. Figure 12 shows the SEM image of the fiber tip and the measured intensities in different RI media. The intensity sensitivity could reach up to 8000% per RI unit.

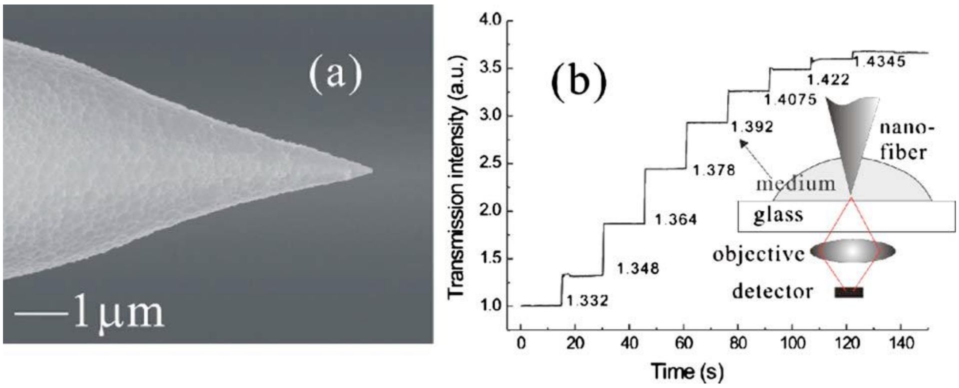

Figure 12. (**a**) SEM image of the fiber tip modified by the etching method; (**b**) measured intensities in different RI media [197].

A series of different micro-hole fiber structures were then fabricated by Donlagic et al. using etching method [198–201]. In these works, purposely produced micro-cell forming fibers (MFF) with phosphorus pentoxide doping were etched by HF acid. Due to different doping areas and the fact that the phosphorus-doped region has a considerably higher etching rate than the pure silica, various micro-structures were formed. The MFF in [198] has elliptical phosphorus-doped region across the fiber. The microcell formed by the etching can be used as a transmission cell or as a miniature FPI for the sensing applications. The MFF in [199] has a slight different structure with the previous one, which keeps the fiber core. The resultant etched structure consists of a thin micro-wire positioned in-between two lead SMFs. The micro-wire waveguide interconnects both SMF cores. The transmission of the micro-structure was monitored for the RI sensing. By coating with thin porous SiO_2 layer, the sensor could also be used for simultaneous RH and temperature measurements [201]. The MFFs in [200] have even larger areas of phosphorus-doped region, which could be etched to form an open FP cavity as well as an in-fiber FP cavity. The sensor has used for the measurement of pressure and RI values. Other examples include chemically etching the multimode graded index fiber for strain and temperature measurement [202], other phosphorus-doped fibers [203,204], and side-hole fiber for microfluidic sensing [205].

An in-line fiber micro-cantilever for vibration sensing was proposed by our group in 2013 for the first time [206]. Due to the unique structure of the bend-insensitive fiber (BIF) consisting of a Germania doped silica core and a pure silica inner-cladding region enveloped by a ring of randomly distributed air-filled nanopockets, the HF acid preferentially etched the ring region, leading to the formation of a suspended fiber core cantilever as shown in Figure 13. The etched BIF was then fused with a readout SMF. Vibration induced periodic bending of the micro-cantilever angularly scans the readout fiber core, which results in output power modulation corresponding to certain driven frequencies and voltages of a shaker. Experiments were conducted with a demonstration of continuous vibration measurement with frequency range of 5 Hz–10 kHz.

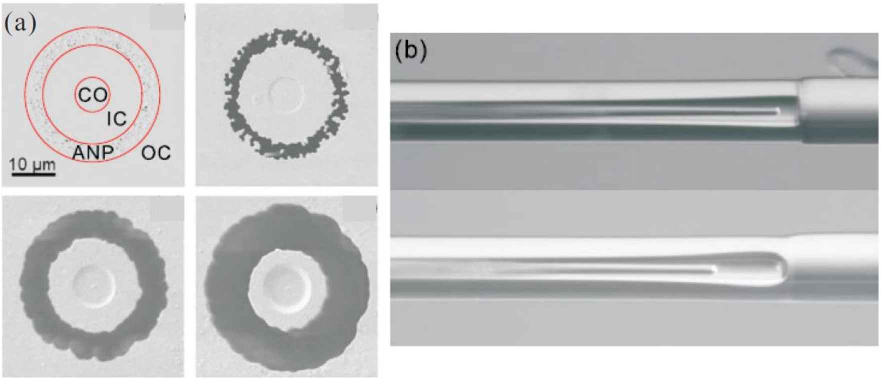

Figure 13. (**a**) SEM images of the transversal cross-section of the bend-insensitive fiber (BIF) after different etching time; (**b**) Optical microscope images of the in-line fiber cantilevers [206].

6.3. Focused Ion Beam (FIB) Micro-Machined Devices

When an ion impinges on a solid, its kinetic energy is lost through the interactions with the sample atoms. This transfer of energy from the ion to the solid leads to different possible processes including ion reflection and backscattering, atomic sputtering and ion emission, sample damage and heating. The focused ion beam uses a set of electromagnetic lenses to focus a beam of ions on the surface of a sample. Compared with the electrons in the SEM technique, the ions have a much larger mass as well as a larger size and thus will eject material from the surface on which they are focused [207]. The FIB technology based on this interaction has proven to be a perfect candidate for micro-machining and nano-fabrication by taking its advantages such as small and controllable spot size in nanometer scale and high beam current density. It is possible to directly fabricate a micro-cavity directly in a sub-wavelength micro-fiber by FIB.

In 2010, Lu et al. used the FIB method to make an air-gap micro-cavity-based FPI in a fiber taper as shown in Figure 14. The fabricated micro-cavity forms a reflective FP modal interferometer, which generates interference among the reflected fundamental mode and excited high-order modes at the end-faces [208,209]. The open micro-cavity provides the access for the RI measurement and could be also used for high-temperature sensing. Then two different FPI structures including an indented FP structure and a cantilever FP structure are fabricated by combining the FIB technique with the chemical etching [210]. The cantilever FP structure was sensitive to vibrations and able to measure frequencies in the range of 1Hz to 40 kHz. Coating was also put onto the FPI walls to increase the mirror reflectivity by a factor of about 26 [211], which has been demonstrated with a high sensitivity on a wide RI measurement range [212]. Recently, a multi-cavity structure was fabricated by the FIB technique by combining the concepts of solid silica cavity and gap cavity [207]. The structure was analyzed using a fast Fourier transform (FFT) method to demultiplex the signals of each cavity. Simultaneous measurement of temperature and RI was then demonstrated.

The FIB technique has recently been utilized to fabricate nano-structured devices for optical trapping applications. The latest advances in the optical trapping based on the self-induced back-action (SIBA) [213] enable to trap the biologically relevant nanoparticles such as proteins. Optical tweezers made from optical fibers have been proved to be an effective tool for the detection, identification, and observation of single nanoparticles. One of the latest typical works was reported by Berthelot et al. in 2014 [214], where a bowtie nano-aperture (BNA) was nano-machined at the tapered fiber tip as shown in Figure 15a,b. In order to prevent light leakage through the sides of the taper cone, the tapered fiber was firstly coated with 200 nm aluminum. Then the tip extremity was cut to obtain a flat facet by using the FIB milling and was subsequently coated with 100 nm gold. Finally, FIB was used again to mill the BNA at the center of the 1-μm diameter gold platform. The fabricated fiber taper-based optical tweezers are capable of detecting and manipulating sub-100-nm dielectric objects over large ranges. In the same year, the BNA was opened through FIB technique at the apex of a metal-coated polymer fiber tip [215]. 3D optical trapping of 0.5 µm latex beads was successfully conducted, which demonstrates that the device has promising applications such as biological and chemical probing and trapping. Similar structures could be found in several following works [216,217]. To overcome the fragility of the fiber taper-based optical trapping devices, a more robust structure was proposed by Gordon et al. by engraving double nanohole aperture at the cleaved fiber end through FIB milling as shown in Figure 15c [218]. An optical transmission increase was observed when single 20 and 40 nm polystyrene spheres were trapped by the device. This compact and robust device is of interest for future biosensor and optical nano-pipette devices.

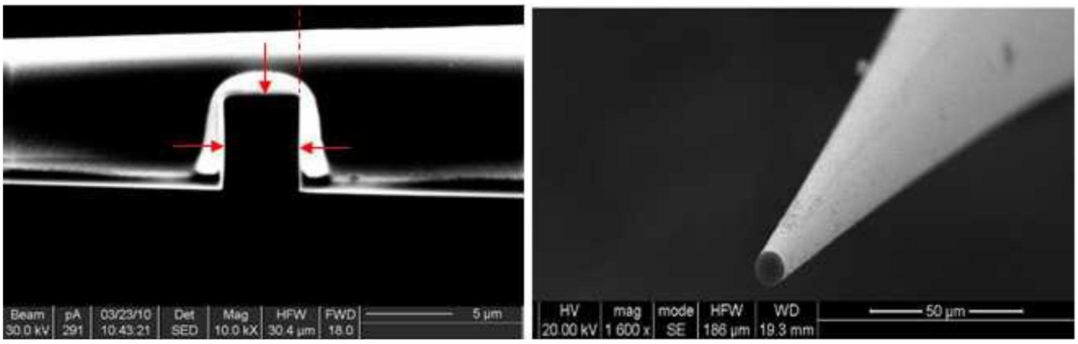

(**a**) (**b**)

Figure 14. SEM images (**a**) of the micro-notch cavity from the side view; (**b**) of the cross section with the fiber tip cleaved at the position indicated in (**a**) by a dash line [208].

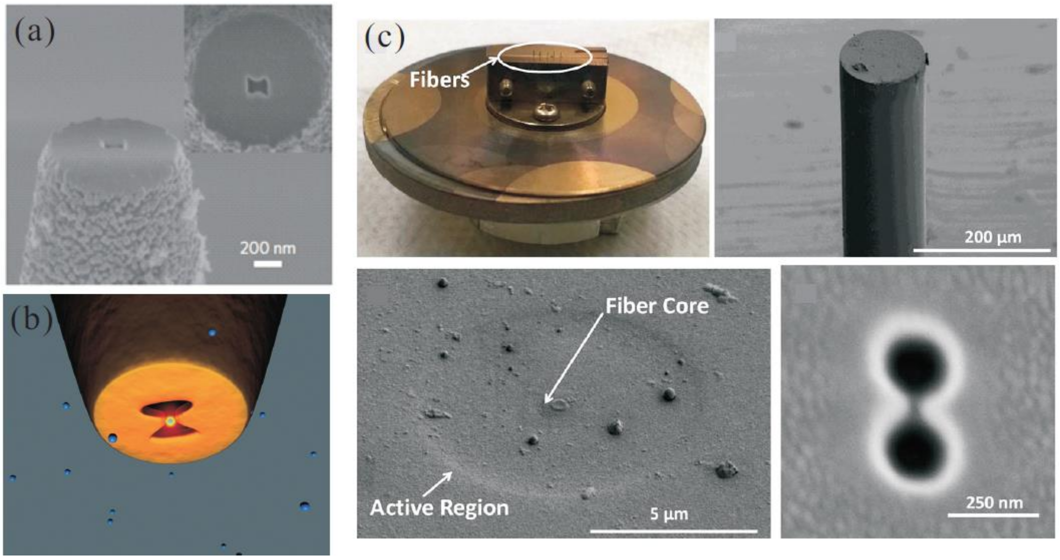

Figure 15. (**a**) SEM image of an 85-nm-gap bowtie nano-aperture (BNA) patterned at the extremity of a tapered optical fiber; (**b**) Schematic of experimental configuration for trapping nano-particle [214]; and (**c**) double nanohole in a cleaved optical fiber end [218].

6.4. Other Methods Based Micro-Machined Devices

Fusion splicing different modified fibers together is another way to construct the micro-machined devices. For example, fusion splicing between an etched graded index MMF and a normal SMF would result in an air hole in the splicing region, which performs as a FPI sensor for RI and temperature measurements [219]. Another easier scheme is splicing a SMF and a PCF as shown in [220].

Due to the collapsed region of the PCF during the splicing process, a micro-FPI was formed. A more straightforward method to obtain an air-gap in the fiber was realized by splicing a thin piece of C-shaped fiber between two SMFs [221]. Arc discharge has been directly applied on the hollow-core fiber to destroy the part of the hollow-core fiber and leave a micro-cavity inside the fiber [222,223]. Curvature, displacement, RI, load, and temperature have been characterized by the proposed sensors. An ultrathin film of gold embedded in the far end of a SMF was also used to construct a compact FPI [224]. The endface of the SMF and the thin film comprised the two mirrors for the FPI, which demonstrates high sensitivity RI and high temperature measurements.

Other interesting micro-machined devices include the ferrule-top micro mechanical sensor and fiber sensors fabricated by multi-photon direct laser writing (DLW). By varying the power of the excitation laser, the static bending of the ferrule-top cantilever could be controlled [225]. The environmental humidity and pressure could be measured by introducing amplitude modulation to excite the vibrations of the device for resonance curve measurement. Various refractive lenses, a compound lens system, and a woodpile photonic crystal within the resin on the end-face of the optical fiber are fabricated by the DLW method [226]. These devices could find applications such as in low insertion-loss micro-laser couplers, high efficiency optical fiber couplers, fiber output beam shapers, and a new class of optical sensors. Recently, a Fabry-Perot micro-optical resonator on the end-face of a SMF was fabricated by DLW. It has been tested for tracing the vapors of common organic solvents [227].

7. Grating-Based Microstructures

Fiber gratings are structures with periodic modulations of the refractive index along the fiber length. The first fiber grating structure is the FBG, which was fabricated in 1978. FBG can reflect particular wavelengths of light and transmit all others by controlling the periodic variation in the refractive index of the fiber core. The periodicity of the RI modification is usually in the scale of the radiation wavelength. FBGs have been widely used as a sensing element in areas including strain sensing, temperature monitoring, underwater acoustic sensing, and rotation sensing. The advantages of FBG sensors include immunity to the electromagnetic interference, inherent self-referencing, lightweight, low cost and possibility for multiplexing. In contrast to the small period of FBG in the scale of sub-microns, LPG has a much larger period in the order of a fraction of a millimeter. LPGs couple copropagating modes with close propagating constants. Due to the large periodicity, LPGs are relatively simpler to manufacture than FBGs. The transmission spectra of LPG have dips at the wavelengths corresponding resonances with various cladding modes. It has been demonstrated that LPG is an effective sensor to separate different measurands simultaneously.

Microfibers with large evanescent fields, strong confinement, configurability, and improving robustness have attracted intensive attention and been considered as an excellent target to write gratings on. The strong evanescent field and tiny size have facilitated the microfiber-based gratings as miniature refractive index sensors. Furthermore, only small amounts of fused silica need to be removed when manufacturing gratings along the microfiber, which makes them easy to fabricate. Despite the periodic index modifications imposed on fibers to make FBG and LPG, random modifications of refractive index has been explored and executed on fibers, which introduces new properties and sensing capabilities to the grating configurations.

7.1. Microfiber-Based Fiber Bragg Grating

Several techniques have been employed so far for the fabrication of microfiber-based FBG, which includes excimer laser irradiated FBG, femtosecond laser irradiated FBG, focused ion beam milled FBG, and other techniques. Due to the much lower diameter of microfiber, the index contrast of the microfiber-based FBG is usually much higher [127].

The earliest work using excimer laser to fabricate FBG on the microfiber was proposed in 2005 [228]. With the help of the wet-chemical etching setup using hydrofluoric (HF) acid, the diameter of the fiber was reduced to 6 μm as shown in Figure 16a. Then a KrF excimer laser and a phase mask were used to write FBG along the etched fiber and the sensor was used for RI measurement of surrounding liquid. In 2010, FBGs were written on microfibers having different diameters as shown in Figure 16b [229]. One higher mode was excited through the microfiber, resulting two reflection peaks alongside with the core mode. It was noted that the higher order mode was more sensitive to the surrounding RI variations than the fundamental mode. More reflection peaks were observed in a following work in 2011 [230], where the inscription of FBGs were made by 193 nm ArF excimer laser on microfibers with diameters from tens of μm to 3.3 μm without hydrogen loading or other treatment for photosensitization. Four reflection peaks were observed, three of which correspond to high order mode resonances. The microfiber-based FBG has been also used as a miniature contact force sensor [231] with an extremely high sensitivity of 1.37 mN and excellent linearity up to a contact force of 0.65 N. High-efficiency inscription of FBG has been achieved on a microfiber drawn from the standard MMF [232]. A sufficient overlap between the fundamental mode and the induced refractive index modulation region is provided by the enlarged photosensitive core offered by the MMF, which remarkably enhances the efficiency of grating inscription. Another microfiber-based FBG was fabricated on a tapered SMF with two short transition regions [233], which has been demonstrated as a temperature-compensated RI sensor. Hydrogen sensors based on microfiber FBG was also proposed in [234], where the microstructure was coated with palladium coatings. The reflection peak could shift by −1.08 nm when the sensor was exposed to the hydrogen with a concentration of 5%, as a result of the evanescent field interacting with the palladium film.

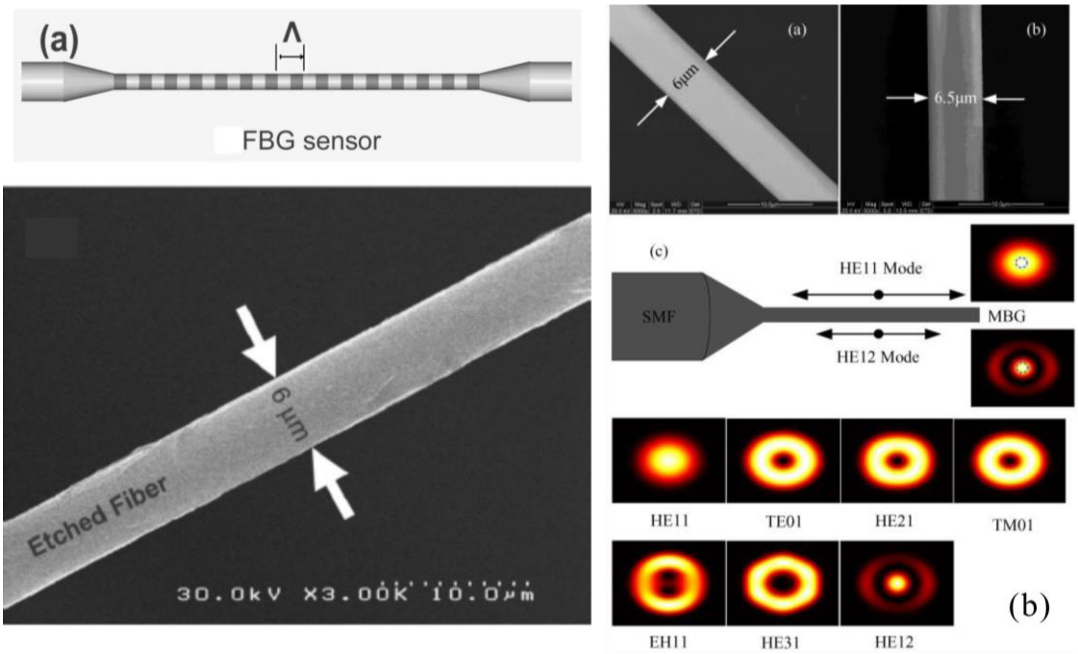

Figure 16. (**a**) Schematic and SEM image of microfiber-based fiber Bragg grating (FBG) [228]; (**b**) SEM images of microfiber-based FBGs and the schematic diagram of the operation principle of mode coupling in the microfiber-based FBG [229].

Femtosecond (fs) laser is another commonly used tool for the grating fabrication. A high-quality retroreflecting FBG written by fs laser in standard SMFs was first achieved in 2003 by Mihailov et al. [235]. In 2006, Grobnic et al. wrote FBGs in the waist of a biconical tapered fiber and a tapered fiber tip using an fs laser source and a phase mask [236]. The periodic refractive index modulation was made in both the core and cladding of the tapered region. The evanescent field in the taper interacts with the ambient environment and the intensity of the reflected signal was used to measure the refractive index changes of the ambient environment as low as 2.5×10^{-5}.

The device was also demonstrated as a fluid level sensor. In 2010, the RI sensing performance of the microfiber-based FBG written by fs laser was further studied [237]. It was found that the RI sensitivity depends on the microfiber diameter and a smaller diameter corresponds to a large sensitivity. A unique microfiber-based FBG was fabricated in 2012 by using phase mask technique and fs laser ablation to drill periodic nanoholes in microfibers [238]. The diameters of these nanoholes ranged from 400 to 550 nm and the depths up to 800 nm. The formed high-index-contrast FBG showed transmission dips down to −23 dB and 3 dB bandwidth of 1.14 nm. The grating reflectivity was also enhanced by 3 dB. Recently, the FBG was written in a microfiber, which was sandwiched between two standard SMFs [239]. The sandwiched structure formed a MZI, which was utilized for simultaneous RI and temperature measurements together with the FBG written in the microfiber. The microfiber-based FBG was then molded with acetal to enhance the temperature sensitivity up to 479.48 pm/°C [240].

Microfiber-based FBGs were also fabricated using the focused ion beam (FIB) milling technique in several works. A typical example is the work conducted by Tong et al. in 2011 [241], where 100 nm-depth grooves were etched by FIB on the surface of the silica microfibers with diameters less than 2 μm. The microfiber-based FBG showed a transmission dip of up to 15 dB and was used for RI measurement with sensitivity of 660 nm/RIU. Another device using the same fabrication technique was a 61-period FBG with 200 nm-deep shallow grooves on a tapered fiber [242]. The compact sensor was able to survive in high temperature up to 500 °C with a temperature sensitivity of 20 pm/°C. Biconcave air cavities with a period of 506 nm were curved-out along the waist of a micro-tapered fiber using the FIB system in [243]. Before the FBG fabrication, the microfiber was partly embedded in the low RI polymer and a 100 nm layer of gold was deposited on the taper surface to avoid charging during the FIB milling. This compact device can find applications in many fields such as temperature and RI sensing and optical communications.

The inscription of FBG in chalcogenide wires with sub-wavelength diameter was also proposed and demonstrated in 2011 [244]. He-Ne laser with a modified transverse holographic method was employed to write grating in the 1550 nm band. The grating spectrum reaches an extinction ratio of 40 dB. The micro-device was considered excellent candidate for applications in sensing and nonlinear area and for mid-infrared light processing. Polymer microfiber was also inscribed with FBG in [245]. A He-Cd laser was used for the FBG writing on the 16 μm diameter microfiber, resulting a maximum reflectivity of 5%. Temperature and strain characterizations were performed using the microfiber FBG with different diameters.

The FBG regions written along the microfiber could also be wrapped by the monolayer graphene to form the grating cladding [246]. The graphene is an ultrathin waveguide with complex permittivity, which would enhance the surface evanescent fields. The reflection spectra of the graphene FBG could be easily modified by choosing a microfiber with proper diameter and alternating the refractive index of graphene. Such all-fiber-based graphene Bragg gratings with low insertion loss and tunability would pave a new way for the applications of graphene-based devices including tunable filters, sensors, fiber lasers and wavelength converters. Chemical gas sensing was realized by taking advantage of the enhanced surface field of the graphene coated FBG with an ultrahigh sensitivity of 0.2 and 0.5 ppm for NH3 and xylene gas, which are ten times higher than the FBG without graphene coating [247]. The fast responses of the compact structure facilitate the applications in high sensitivity gas sensing and trace analysis.

7.2. Microfiber-Based Long-Period Fiber Grating

LPGs are also of great interest in microfiber-based devices. As early as in 2005, Allsop et al. [248] reported writing a single LPG in a biconical fiber taper, resulting in an interferometric fiber sensor that provides a resolution of 10^{-4} for RI measurements. Modeling of microfiber-based LPG was performed in 2006 by taking into account the fiber taper geometry as well as the coupling to the local cladding modes by the LPG itself [249]. A new spectral bifurcation effect in the microfiber-based LPG was observed and the device has been demonstrated with a greater spectral sensitivity with respect to RI in the 1.333 range than other fiber grating sensors. CO_2 laser and fs laser have been utilized for the fabrication of the LPG in microfiber in 2009 by Jin et al., respectively. High frequency CO_2 laser pulses were focused on 6.3 µm silica microfibers and periodically modified the transverse dimension of the fiber [250], leading to a 20-period LPG with a 27 dB attenuation dip. Fs IR laser was also used to periodically modify the surface of the microfibers with diameters from 1.5 to 3 µm [251]. The written LPGs have grating periods of a few tens of microns, which are much smaller than those in the conventional fibers. The compact device with 10-period LPG of only 150 µm length demonstrated a strong resonance dip of more than 20 dB around 1330 nm.

A novel structural LPG made from the microfiber was proposed in 2012 [252]. One microfiber was helically coiled onto another microfiber with relatively thicker diameter. The coiled microfiber was able to periodically modulate the evanescent field of the straight microfiber, leading to a resonance transmission notch of 16.2 dB. A unique double-clad fiber with boron and germanium co-doped inner cladding was also used to fabricate the microfiber-based LPG [253]. This co-doped area enhanced the UV photosensitivity of the fiber, which makes it suitable for inscribing grating into the taper region. Another innovative technique was employed to manufacture the LPG on the fiber taper in [254]. The LPGs were made by periodically pulling and elongating the tapered fiber. Thus, the periodic formation of the locally tapered diameter changed the effective RI, leading to the realization of the LPG structures. Two LPGs were also inscribed in the silica microfiber in order to form a MZI [255]. Owing to the large effective index difference between the fundamental and higher order modes, the LPG-based MZI could be more compact with less than 1cm in length. A point-by-point dip coating method was also utilized to fabricate the microfiber-based LPG in [256]. The grating structure was fabricated by periodically immersing the microfiber into a miniature polydimethylsiloxane droplet, which is suspended at the end-tip of the SMF with the help of a high precision 3D translation stage. A 10-period LPG with a grating period of 143 µm was demonstrated with a resonant dip of 19 dB. LPG was also successfully inscribed in the polymer functionalized optical microfiber, as reported recently in [257]. This small footprint and compact device showed high sensitivity for strain and axial force measurements and the temperature sensitivity could be increased with appropriate sealing.

7.3. Random Fiber Gratings

Recently, there has been an increasing interest in the design and fabrication of random fiber gratings. In 2008, Derevyanko theoretically studied the statistics of the reflection spectrum of a short-correlated disordered FBG [258]. It was found that by pseudo-randomly modulating the RI in segments with scale larger than the correlation length, a flat-top reflection spectrum could be achieved with fewer side-lobes outside the band gap than the spectrum of a uniform grating. In 2015, Yin et al. successfully fabricated a top-hat FBG by employing the phase noise and pseudorandom variations of the refractive index [259]. The flatness of the bandwidth can be controlled by the correlation length of the noise. The hat height and width could be adjusted by the apodization, grating index, and grating length. It was not until recently that the random grating is fabricated for optical sensing applications. Xu et al. [260] reported a novel multi-parameter fiber optic sensor based on an fs laser micro-machined random grating to realize simultaneous measurement of temperature, axial strain, and surrounding RI. This novel random grating was manufactured by the fs laser modification processed spot by spot with random separations ranging from 0 to 3.5 µm without phase mask and critical alignment and vibration control as shown in Figure 17. The phase variation induced spectral shift responding to different external disturbances were extracted by adopting a wavelength-division spectral cross-correlation algorithm. The developed sensor can be potentially applicable in areas of engineering, biomedical, biological, and environmental sensing with its robust physical strength and high sensitivities. Besides the optical sensing application, the fabricated fiber random grating has been also applied as a random feedback medium for the realization of a low-noise Brillouin random fiber laser [261].

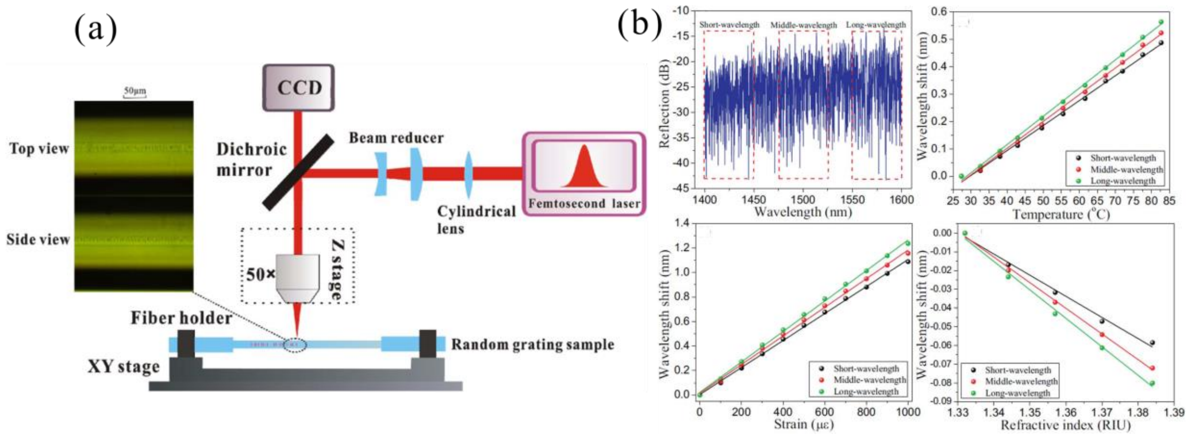

Figure 17. (**a**) Experimental setup of the fs laser micro-machining system with microscopic images of the fiber random grating samples; (**b**) Three spectrum subsections selected in the reflection spectrum of fiber-optic random grating; cross-correlation peak wavelength shift calibration results for temperature, strain, and refractive index [260].

8. Mode-Mismatched and Hybrid Micro-Structured Devices

8.1. Mode Mismatched Micro-Structured Devices

Other groups of micro-structured fiber optic sensors include the mode-mismatched and hybrid micro-structured devices. Two frequently employed ways have been used for manufacturing the mode-mismatched micro-structured fiber optic sensor: by splicing fibers with different core-cladding structures together or by deliberately splicing two sections of fibers with an offset. The purposes of either way are to introduce the mismatch between the mode field distributions of lead-in fiber and lead-out fiber, which spreads the energy of the core mode from the lead-in fiber out to the cladding region of the lead-out fiber. An interferometric sensor is formed by concatenating two mode-mismatched splicing with one for the excitation of cladding modes and the other for the coupling back of cladding modes.

The most typical mode-mismatched micro-structured sensor is to sandwich a section of MMF between two SMFs to form a SMF-MMF-SMF (SMS) structure. As early as 2003, Kumar et al. [262] studied the transmission characteristics of the SMS fiber optic sensor structures. It was found that if the spot sizes of the fundamental modes of the single and MMFs do not match with each other, the transmitted power would be highly sensitive to the operation wavelength and the length of the MMF. In 2009, the critical wavelength shifts of the transmission spectrum of the SMS structure was monitored for temperature and strain measurements [263]. MMFs with different doping materials were studied, demonstrating spectral shifts in different directions. Later, the RI sensing performance of the SMS structure and the SMS structure with tapered MMF were investigated in [264]. Numerical simulations of the light propagation in the structures are performed by employing a wide-angle beam propagation method in cylindrical coordinates and it was reported that the SMS with tapered MMF could be exploited for measuring a broad RI range with high resolution. A thinned fiber was also inserted into the SMS structure between the MMF and SMF [265], which was successfully employed for water level and surrounding RI measurements.

The SMS could be also modified by replacing the central MMF with other kinds of fiber with different core structures from the SMF. A thin core fiber (TCF) was sandwiched between two SMFs in the work reported in [266]. As shown in Figure 18a, instead of an in-line MZI, the new device formed an in-line MI. The sensor was tested with a high sensitivity for RI measurement and was insensitive to the temperature variation. PCF was also utilized to replace the MMF in [267] as shown in Figure 18b. The air-hole region of the PCF was collapsed when exposed under the electric arc of the fusion splicer, making this region no longer a single mode fiber since the PCF has no cladding layer. Thus, some parts of the beam that were originally in the core mode can be coupled to several cladding modes, providing the access to form the in-line MZI. Similar structure was fabricated in [268] with a high temperature measurement up to 100 °C. High-order-mode fiber (HOMF) was also fusion spliced between two SMFs to form an in-line MZI [269]. The dispersion effects of the HOMF were utilized to effectively discriminate different environmental disturbances by monitoring the phase shifts of multiple dispersion peaks. Another interesting structure is to sandwich a section of SMF between two MMFs as reported in [270,271]. Refractive index and curvature have been measured using the proposed MMF-SMF-MMF structures.

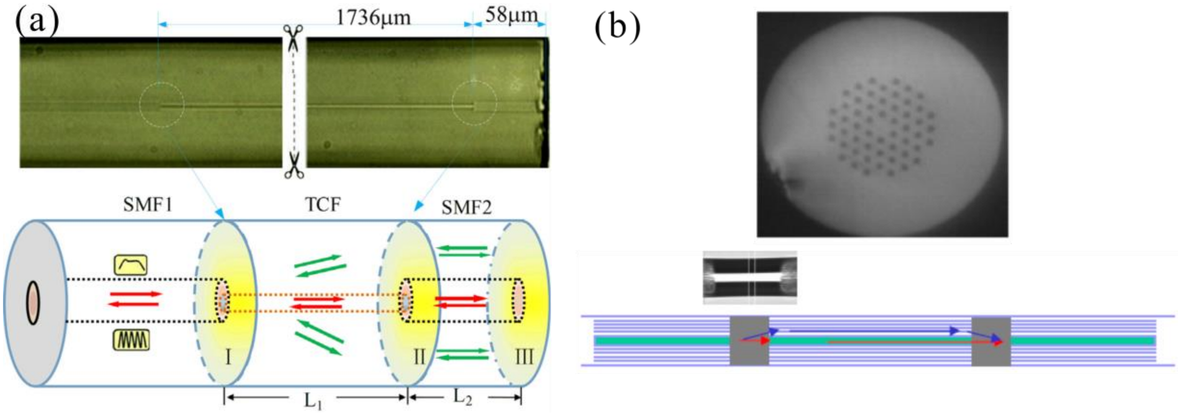

Figure 18. (**a**) Microscope image and schematic diagram of the SMF-thin core fiber (TCF)-SMF structure [266]; (**b**) Schematic of the SMF-PCF-SMF structure and the cross sectional view of the PCF [267].

Offset splicing is another technique for manufacturing the mode mismatched micro-structure fiber optic sensors. MZI and MI could be realized by making two offset splicing and one offset splicing combined with fiber end-face coating [272]. The offset splicing deliberately introduces a core offset between the two sections of fibers, leading to that part of the energy in the core mode from the lead-in fiber will be spread out to the cladding region of the lead-out fiber. The fabricated Michelson-type interferometer is more compact considering only one end access for light is needed. A similar Michelson-type interferometer was fabricated by the offset splicing technique in [273]. The sensor was reported with high RI sensitivity of 1.24×10^{-4}/RIU and 8.35×10^{-5}/RIU at RI of 1.3350 and 1.3845. Displacement and curvature measurements were also achieved by the mismatched microstructures made by offset splicing as reported in [274,275]. Also, the offset spliced structure could be modified by replacing the SMF with other fibers. In [276], thin core fiber (TCF) was offset spliced with a SMF to form a MI. The proposed sensor was insensitive to the temperature change and had high sensitivity for RI sensing.

8.2. Hybrid Micro-Structured Devices

To date, several techniques including tapering, offset splicing, FBG/LPG inscription, and laser micromachining have been proposed for the fabrication of micro-structured fiber-optic sensors. It has been demonstrated that each of these techniques when employed alone can be an effective method for the manufacturing of the micro-structured devices. Furthermore, by combining different micro-machining techniques together, devices with excellent performances could also be obtained.

It is well-known that two light steering elements are able to comprise an in-line MZI. Fiber abrupt taper, offset splicing, FBG/LPG, and laser micro-machined spot have been acted as the light steering elements. Combinations of these microstructures are able to achieve the fiber-optic interferometric sensors as well.

Abrupt fiber taper has been concatenated with FBG [277], LPG [278], offset splicing [279,280], and laser micro-machined spot [281]. In [277], a FBG was inscribed in an abrupt taper. The core mode was partially coupled into the cladding by the abrupt taper and the FBG in the abrupt taper coupled light from the cladding to the backward-propagating core mode, forming an interferometric cavity. Curvature and displacement measurements were conducted by the sensor. In [278], an LPG was cascaded with an abrupt taper, which was utilized as an inclinometer. The axis of rotation went through the center of the taper, which affected the coupling of the core mode to the cladding modes when the curvature was changed. In [279], the combined abrupt taper and offset splicing between two SMFs were used for the simultaneous axial strain and temperature measurement. RI sensing was also realized in a similar structure reported in [280]. In [281], the abrupt taper was combined with a micro-machined spot fabricated by an fs laser. The device was able to measure temperature, axial strain, and RI. Another structure was fabricated by tapering the central fiber which was previously offset spliced with two sections of SMFs [282]. The tapered fiber section enhanced the sensitivity of the RI measurement. Other similar structures include the up taper cascaded with offset splicing [283] and FBG [284] for bending vector and displacement measurements.

The splicing between the SMF and MMF and the offset splicing between two SMFs have been combined together to form an interferometric sensor as reported in [285]. A more complicated structure was made by inscribing an FBG into one section of the SMFs [286]. Simultaneous measurements of temperature and strain or temperature and curvature were realized by the proposed sensor. Another complex structure was achieved by concatenating the fiber taper, offset splicing, and FBG to obtain an inter-modal interferometer [287]. By using the temperature sensing properties of FBG, the temperature-compensated liquid level measurement was achieved by the sensor. The two splicing points of the SMF-PCF-SMF structure were also regularly tapered [288] and up-tapered [289]. The tapered splicing points further enhanced the sensitivity of the refractive index measurements.

More complex hybrid micro- or nano-structured devices such as nano-layered micro-structured fiber devices, LPGs within D-shaped fibers, carbon nanotubes integration with fibers, function materials integration in micro-optic fibers, hybrid metallo-dielectric nanostructures on fiber facet could be found in [290,291].

9. Future Prospects

There is no doubt that designs and fabrications of novel micro-structured fiber optic sensors will continue to be a booming research area with the development of micro- and nano-technology and creation of fibers with novel optical properties. Challenges and opportunities coexist in the future work concerning the micro-structured fiber optic sensors, which include (1) Capability of sensing selectivity and simultaneous multi-parameter measurement: although to date several micro-structured fiber optic sensors with dual-parameter measuring ability have been proposed, efforts should be put into the minimization of the error of the simultaneous multi-parameter measurements and expanding dual-parameter measurement to three-parameter or even more parameter characterizations as crosstalk effect is usually caused by more than two parameters in real practices; (2) Even higher sensitivity: as more precise measurements are highly desired in chemical and biomedical fields such as single molecule detection and gas sensing, micro-structured fiber optic sensors with extremely high sensitivities and accuracies are preferred; (3) Intelligence and flexibility: an intelligent micro-structured fiber optic sensor should be able to have adjustable and changeable functions when facing different target samples and situations. A more flexible architecture of sensor would be more applicable and powerful; (4) Sensing in harsh environments, such as in extremely low/high temperature, high pressure, high radiation, and high humidity; (5) Long-term stability and package protection: as the robustness of the tiny structures is the key to the sensing performance and durability of the device, a better package without any cost of sensitivity will be the future aim.

10. Conclusions

This review paper presents a comprehensive and systematic overview of the various micro-structured optical fiber sensors regarding their working principles, waveguide structures, fabrication and manufacturing process, sensing applications and performances, as well as state of the art development. The advantages of the micro-structured fiber sensors over the conventional counterparts include easy fabrication and mass-production, low cost, good reproducibility and excellent optical performance. It is believed that a substantial portion of the micro-structured fiber-optic sensors are capable of being commercialized and put into practice in the near future. Future work should focus on the optimization of the sensor's functionalities for different applications, long term stability and better package for protection issues.

Acknowledgments: The authors acknowledge the Canada Research Chair Program (CRC in Fiber Optics and Photonics) and the Natural Sciences and Engineering Research Council of Canada (NSERC) Discovery Grant.

Author Contributions: The paper was written by Yanping Xu and revised by Xiaoyi Bao, Liang Chen and Ping Lu.

Conflicts of Interest: The authors declare no conflict of interest.

References

1. Mescia, L.; Prudenzano, F. Advances on optical fiber sensors. *Fibers* **2013**, *2*, 1–23. [CrossRef]
2. Giallorenzi, T.G.; Bucaro, J.A.; Dandridge, A.; Sigel, G.; Cole, J.H.; Rashleigh, S.C.; Priest, R.G. Optical fiber sensor technology. *IEEE Trans. Microw. Theory Tech.* **1982**, *30*, 472–511. [CrossRef]
3. Lee, B. Review of the present status of optical fiber sensors. *Opt. Fiber Technol.* **2003**, *9*, 57–79. [CrossRef]
4. Grattan, K.; Sun, T. Fiber optic sensor technology: An overview. *Sens. Actuators A Phys.* **2000**, *82*, 40–61. [CrossRef]
5. Kersey, A.D. A review of recent developments in fiber optic sensor technology. *Opt. Fiber Technol.* **1996**, *2*, 291–317. [CrossRef]
6. Rao, Y.-J. In-fibre Bragg grating sensors. *Meas. Sci. Technol.* **1997**, *8*, 355. [CrossRef]
7. Kersey, A.; Jackson, D.; Corke, M. A simple fibre Fabry-Perot sensor. *Opt. Commun.* **1983**, *45*, 71–74. [CrossRef]
8. Rao, Y.-J. Recent progress in fiber-optic extrinsic Fabry-Perot interferometric sensors. *Opt. Fiber Technol.* **2006**, *12*, 227–237. [CrossRef]
9. Kao, T.; Taylor, H. High-sensitivity intrinsic fiber-optic Fabry-Perot pressure sensor. *Opt. Lett.* **1996**, *21*, 615–617. [CrossRef] [PubMed]
10. Lee, B.H.; Kim, Y.H.; Park, K.S.; Eom, J.B.; Kim, M.J.; Rho, B.S.; Choi, H.Y. Interferometric fiber optic sensors. *Sensors* **2012**, *12*, 2467–2486. [CrossRef] [PubMed]
11. Xu, Y. Multi-Parameter Sensing Based on in-Line Mach-Zehnder Interferometer. Master's Thesis, Université d'Ottawa/University of Ottawa, Ottawa, ON, Canada, 2013.
12. Jha, R.; Villatoro, J.; Badenes, G.; Pruneri, V. Refractometry based on a photonic crystal fiber interferometer. *Opt. Lett.* **2009**, *34*, 617–619. [CrossRef] [PubMed]
13. Allsop, T.; Reeves, R.; Webb, D.J.; Bennion, I.; Neal, R. A high sensitivity refractometer based upon a long period grating Mach-Zehnder interferometer. *Rev. Sci. Instrum.* **2002**, *73*, 1702–1705. [CrossRef]
14. Rao, Y.-J.; Ran, Z.-L. Optic fiber sensors fabricated by laser-micromachining. *Opt. Fiber Technol.* **2013**, *19*, 808–821. [CrossRef]
15. Machavaram, V.; Badcock, R.; Fernando, G. Fabrication of intrinsic fibre Fabry–Perot sensors in silica fibres using hydrofluoric acid etching. *Sens. Actuators A Phys.* **2007**, *138*, 248–260. [CrossRef]
16. Brambilla, G. Optical fibre nanowires and microwires: A review. *J. Opt.* **2010**, *12*, 043001. [CrossRef]
17. Tong, L.; Zi, F.; Guo, X.; Lou, J. Optical microfibers and nanofibers: A tutorial. *Opt. Commun.* **2012**, *285*, 4641–4647. [CrossRef]
18. Brambilla, G.; Xu, F.; Horak, P.; Jung, Y.; Koizumi, F.; Sessions, N.P.; Koukharenko, E.; Feng, X.; Murugan, G.S.; Wilkinson, J.S. Optical fiber nanowires and microwires: Fabrication and applications. *Adv. Opt. Photonics* **2009**, *1*, 107–161. [CrossRef]

19. Amnon, Y.; Yeh, P. *Optical Electronics in Modern Communications*, 5th ed.; Oxford University Press: New York, NY, USA, 1997.
20. Tsao, C. *Optical Fibre Waveguide Analysis*, 1st ed.; Oxford University Press: New York, NY, USA, 1992.
21. Fielding, A.J.; Edinger, K.; Davis, C.C. Experimental observation of mode evolution in single-mode tapered optical fibers. *J. Lightwave Technol.* **1999**, *17*, 1649–1656. [CrossRef]
22. Black, R.; Bourbonnais, R. Core-mode cutoff for finite-cladding lightguides. *IEE Proc. J* **1986**, *133*, 377–384. [CrossRef]
23. Kou, J.-L.; Ding, M.; Feng, J.; Lu, Y.-Q.; Xu, F.; Brambilla, G. Microfiber-based Bragg gratings for sensing applications: A review. *Sensors* **2012**, *12*, 8861–8876. [CrossRef] [PubMed]
24. Love, J.; Henry, W.; Stewart, W.; Black, R.; Lacroix, S.; Gonthier, F. Tapered single-mode fibres and devices. I. Adiabaticity criteria. *IEE Proc. J.* **1991**, *138*, 343–354.
25. Little, B.E.; Laine, J.-P.; Haus, H.A. Analytic theory of coupling from tapered fibers and half-blocks into microsphere resonators. *J. Lightwave Technol.* **1999**, *17*, 704. [CrossRef]
26. He, Y.; Shi, F.G. A graded-index fiber taper design for laser diode to single-mode fiber coupling. *Opt. Commun.* **2006**, *260*, 127–130. [CrossRef]
27. Corres, J.M.; Arregui, F.J.; Matias, I.R. Design of humidity sensors based on tapered optical fibers. *J. Lightwave Technol.* **2006**, *24*, 4329–4336. [CrossRef]
28. Niu, L.; Zhao, C.-L.; Gong, H.; Li, Y.; Jin, S. Curvature sensor based on two cascading abrupt-tapers modal interferometer in single mode fiber. *Opt. Commun.* **2014**, *333*, 11–15. [CrossRef]
29. Xu, L.; Jiang, L.; Wang, S.; Li, B.; Lu, Y. High-temperature sensor based on an abrupt-taper Michelson interferometer in single-mode fiber. *Appl. Opt.* **2013**, *52*, 2038–2041. [CrossRef] [PubMed]
30. Li, B.; Jiang, L.; Wang, S.; Zhou, L.; Xiao, H.; Tsai, H.-L. Ultra-abrupt tapered fiber Mach-Zehnder interferometer sensors. *Sensors* **2011**, *11*, 5729–5739. [CrossRef] [PubMed]
31. Tian, Z.; Yam, S.S.-H.; Barnes, J.; Bock, W.; Greig, P.; Fraser, J.M.; Loock, H.-P.; Oleschuk, R.D. Refractive index sensing with Mach–Zehnder interferometer based on concatenating two single-mode fiber tapers. *IEEE Photonics Technol. Lett.* **2008**, *20*, 626–628. [CrossRef]
32. Tian, Z.; Yam, S.-H. In-line abrupt taper optical fiber Mach-Zehnder interferometric strain sensor. *IEEE Photonics Technol. Lett.* **2009**, *3*, 161–163. [CrossRef]
33. Monzon-Hernandez, D.; Martinez-Rios, A.; Torres-Gomez, I.; Salceda-Delgado, G. Compact optical fiber curvature sensor based on concatenating two tapers. *Opt. Lett.* **2011**, *36*, 4380–4382. [CrossRef] [PubMed]
34. Lu, P.; Lin, G.; Wang, X.; Chen, L.; Bao, X. Lateral stress detection using a tapered fiber Mach-Zehnder interferometer. *IEEE Photonics Technol. Lett.* **2012**, *24*, 2038–2041.
35. Hsu, J.-M.; Lee, C.-L.; Chang, H.-P.; Shih, W.C.; Li, C.-M. Highly sensitive tapered fiber Mach-Zehnder interferometer for liquid level sensing. *IEEE Photonics Technol. Lett.* **2013**, *25*, 1354–1357. [CrossRef]
36. Wang, Q.; Wei, W.; Guo, M.; Zhao, Y. Optimization of cascaded fiber tapered Mach–Zehnder interferometer and refractive index sensing technology. *Sens. Actuators B Chem.* **2016**, *222*, 159–165. [CrossRef]
37. Li, Y.; Harris, E.; Chen, L.; Bao, X. Application of spectrum differential integration method in an in-line fiber Mach-Zehnder refractive index sensor. *Opt. Express* **2010**, *18*, 8135–8143. [CrossRef] [PubMed]
38. Harris, E.; Li, Y.; Chen, L.; Bao, X. Fiber-optic Mach-Zehnder interferometer as a high-precision temperature sensor: Effects of temperature fluctuations on surface biosensing. *Appl. Opt.* **2010**, *49*, 5682–5685. [CrossRef] [PubMed]
39. Li, Y.; Chen, L.; Harris, E.; Bao, X. Double-pass in-line fiber taper Mach-Zehnder interferometer sensor. *IEEE Photonics Technol. Lett.* **2010**, *22*, 1750–1752. [CrossRef]
40. Lee, C.-L.; Shih, W.-C.; Hsu, J.-M.; Horng, J.-S. Asymmetrical dual tapered fiber Mach-Zehnder interferometer for fiber-optic directional tilt sensor. *Opt. Express* **2014**, *22*, 24646–24654. [CrossRef] [PubMed]
41. Lu, P.; Men, L.; Sooley, K.; Chen, Q. Tapered fiber Mach-Zehnder interferometer for simultaneous measurement of refractive index and temperature. *Appl. Phys. Lett.* **2009**, *94*, 131110. [CrossRef]
42. Chen, T.; Chen, R.; Lu, P.; Chen, Q.; Chen, K.P. Tapered fibre Mach-Zehnder interferometer for simultaneous measurement of liquid level and temperature. *Electron. Lett.* **2011**, *47*, 1093–1095. [CrossRef]
43. Tian, Z.; Yam, S.S.; Loock, H.-P. Refractive index sensor based on an abrupt taper Michelson interferometer in a single-mode fiber. *Opt. Lett.* **2008**, *33*, 1105–1107. [CrossRef] [PubMed]
44. Amaral, L.; Frazão, O.; Santos, J.; Ribeiro, A.L. Fiber-optic inclinometer based on taper Michelson interferometer. *IEEE Sens. J.* **2011**, *11*, 1811–1814. [CrossRef]

45. Lu, P.; Harris, J.; Xu, Y.; Lu, Y.; Chen, L.; Bao, X. Simultaneous refractive index and temperature measurements using a tapered bend-resistant fiber interferometer. *Opt. Lett.* **2012**, *37*, 4567–4569. [CrossRef] [PubMed]
46. Harris, J.; Lu, P.; Larocque, H.; Xu, Y.; Chen, L.; Bao, X. Highly sensitive in-fiber interferometric refractometer with temperature and axial strain compensation. *Opt. Express* **2013**, *21*, 9996–10009. [CrossRef] [PubMed]
47. Harris, J.; Lu, P.; Larocque, H.; Chen, L.; Bao, X. In-fiber Mach-Zehnder interferometric refractive index sensors with guided and leaky modes. *Sens. Actuators B Chem.* **2015**, *206*, 246–251. [CrossRef]
48. Xu, Y.; Lu, P.; Qin, Z.; Harris, J.; Baset, F.; Bhardwaj, V.R.; Bao, X. Vibration sensing using a tapered bend-insensitive fiber based Mach-Zehnder interferometer. *Opt. Express* **2013**, *21*, 3031–3042. [CrossRef] [PubMed]
49. Chen, N.-K.; Hsieh, Y.-H.; Lee, Y.-K. Tapered fiber Mach-Zehnder interferometers for vibration and elasticity sensing applications. *Opt. Express* **2013**, *21*, 11209–11214. [CrossRef] [PubMed]
50. Geng, Y.; Li, X.; Tan, X.; Deng, Y.; Yu, Y. High-sensitivity Mach–Zehnder interferometric temperature fiber sensor based on a waist-enlarged fusion bitaper. *IEEE Sens. J.* **2011**, *11*, 2891–2894.
51. Gao, S.; Zhang, W.; Geng, P.; Xue, X.; Zhang, H.; Bai, Z. Highly sensitive in-fiber refractive index sensor based on down-bitaper seeded up-bitaper pair. *IEEE Photonics Technol. Lett.* **2012**, *24*, 1878–1881. [CrossRef]
52. Song, H.; Gong, H.; Ni, K.; Dong, X. All fiber curvature sensor based on modal interferometer with waist enlarge splicing. *Sens. Actuators A Phys.* **2013**, *203*, 103–106. [CrossRef]
53. Zhang, S.; Zhang, W.; Geng, P.; Gao, S. Fiber Mach-Zehnder interferometer based on concatenated down-and up-tapers for refractive index sensing applications. *Opt. Commun.* **2013**, *288*, 47–51. [CrossRef]
54. Wen, X.; Ning, T.; Li, C.; Kang, Z.; Li, J.; You, H.; Feng, T.; Zheng, J.; Jian, W. Liquid level measurement by applying the Mach-Zehnder interferometer based on up-tapers. *Appl. Opt.* **2014**, *53*, 71–75. [CrossRef] [PubMed]
55. Gong, H.; Yang, X.; Ni, K.; Zhao, C.-L.; Dong, X. An optical fiber curvature sensor based on two peanut-shape structures modal interferometer. *IEEE Photonics Technol. Lett.* **2014**, *26*, 22–24. [CrossRef]
56. Pu, S.; Dong, S. Magnetic field sensing based on magnetic-fluid-clad fiber-optic structure with up-tapered joints. *IEEE Photonics J.* **2014**, *6*, 1–6.
57. Kang, Z.; Wen, X.; Li, C.; Sun, J.; Wang, J.; Jian, S. Up-taper-based Mach-Zehnder interferometer for temperature and strain simultaneous measurement. *Appl. Opt.* **2014**, *53*, 2691–2695. [CrossRef] [PubMed]
58. Zhang, L.; Zhang, W.; Chen, L.; Yan, T.; Wang, L.; Wang, B.; Zhou, Q. A fiber bending vector sensor based on M-Z interferometer exploiting two hump-shaped tapers. *IEEE Photonics Technol. Lett.* **2015**, *27*, 1240–1243. [CrossRef]
59. Zhang, C.; Zhao, J.; Miao, C.; Shen, Z.; Li, H.; Zhang, M. High-sensitivity all single-mode fiber curvature sensor based on bulge-taper structures modal interferometer. *Opt. Commun.* **2015**, *336*, 197–201. [CrossRef]
60. Yang, R.; Yu, Y.-S.; Xue, Y.; Chen, C.; Chen, Q.-D.; Sun, H.-B. Single S-tapered fiber Mach-Zehnder interferometers. *Opt. Lett.* **2011**, *36*, 4482–4484. [CrossRef] [PubMed]
61. Yang, R.; Yu, Y.-S.; Chen, C.; Xue, Y.; Zhang, X.-L.; Guo, J.-C.; Wang, C.; Zhu, F.; Zhang, B.-L.; Chen, Q.-D. S-tapered fiber sensors for highly sensitive measurement of refractive index and axial strain. *J. Lightwave Technol.* **2012**, *30*, 3126–3132. [CrossRef]
62. Shi, F.; Wang, J.; Zhang, Y.; Xia, Y.; Zhao, L. Refractive index sensor based on S-tapered photonic crystal fiber. *IEEE Photonics Technol. Lett.* **2013**, *25*, 344–347. [CrossRef]
63. Deng, M.; Liu, D.; Li, D. Magnetic field sensor based on asymmetric optical fiber taper and magnetic fluid. *Sens. Actuators A Phys.* **2014**, *211*, 55–59. [CrossRef]
64. Li, J.; Zhang, W.; Gao, S.; Bai, Z.; Wang, L.; Liang, H.; Yan, T. Simultaneous force and temperature measurement using S fiber taper in fiber Bragg grating. *IEEE Photonics Technol. Lett.* **2014**, *26*, 309–312. [CrossRef]
65. Wu, D.; Zhu, T.; Deng, M.; Duan, D.-W.; Shi, L.-L.; Yao, J.; Rao, Y.-J. Refractive index sensing based on Mach–Zehnder interferometer formed by three cascaded single-mode fiber tapers. *Appl. Opt.* **2011**, *50*, 1548–1553. [CrossRef] [PubMed]
66. Yang, J.; Jiang, L.; Wang, S.; Li, B.; Wang, M.; Xiao, H.; Lu, Y.; Tsai, H. High sensitivity of taper-based Mach–Zehnder interferometer embedded in a thinned optical fiber for refractive index sensing. *Appl. Opt.* **2011**, *50*, 5503–5507. [CrossRef] [PubMed]

67. Zhu, C.-C.; Yu, Y.-S.; Zhang, X.-Y.; Chen, C.; Liang, J.-F.; Liu, Z.-J.; Meng, A.-H.; Jing, S.-M.; Sun, H.-B. Compact Mach-Zehnder Interferometer Based on Tapered Hollow Optical Fiber. *IEEE Photonics Technol. Lett.* **2015**, *27*, 1277–1280. [CrossRef]
68. Latifi, H.; Zibaii, M.I.; Hosseini, S.M.; Jorge, P. Nonadiabatic tapered optical fiber for biosensor applications. *Photonics Sens.* **2012**, *2*, 340–356. [CrossRef]
69. Snyder, A.W.; Love, J. *Optical Waveguide Theory*, 1st ed.; Springer Science & Business Media: Boston, MA, USA, 2012.
70. Tiefenthaler, K.; Lukosz, W. Sensitivity of grating couplers as integrated-optical chemical sensors. *J. Opt. Soc. Am. B* **1989**, *6*, 209–220. [CrossRef]
71. Love, J.; Henry, W. Quantifying loss minimisation in single-mode fibre tapers. *Electron. Lett.* **1986**, *17*, 912–914. [CrossRef]
72. Birks, T.A.; Li, Y.W. The shape of fiber tapers. *J. Lightwave Technol.* **1992**, *10*, 432–438. [CrossRef]
73. Yadav, T.; Narayanaswamy, R.; Bakar, M.A.; Kamil, Y.M.; Mahdi, M. Single mode tapered fiber-optic interferometer based refractive index sensor and its application to protein sensing. *Opt. Express* **2014**, *22*, 22802–22807. [CrossRef] [PubMed]
74. Zibaii, M.; Latifi, H.; Karami, M.; Gholami, M.; Hosseini, S.; Ghezelayagh, M. Non-adiabatic tapered optical fiber sensor for measuring the interaction between α-amino acids in aqueous carbohydrate solution. *Meas. Sci. Technol.* **2010**, *21*, 105801. [CrossRef]
75. Brambilla, G.; Finazzi, V.; Richardson, D. Ultra-low-loss optical fiber nanotapers. *Opt. Express* **2004**, *12*, 2258–2263. [CrossRef] [PubMed]
76. Wang, X. Characterization of Fiber Tapers for Fiber Devices and Sensors. Ph.D. Thesis, University of Ottawa, Ottawa, ON, Canada, 2012.
77. Sumetsky, M.; Dulashko, Y.; Hale, A. Fabrication and study of bent and coiled free silica nanowires: Self-coupling microloop optical interferometer. *Opt. Express* **2004**, *12*, 3521–3531. [CrossRef] [PubMed]
78. Shi, L.; Chen, X.; Liu, H.; Chen, Y.; Ye, Z.; Liao, W.; Xia, Y. Fabrication of submicron-diameter silica fibers using electric strip heater. *Opt. Express* **2006**, *14*, 5055–5060. [CrossRef] [PubMed]
79. Zhang, E.J.; Sacher, W.D.; Poon, J.K. Hydrofluoric acid flow etching of low-loss subwavelength-diameter biconical fiber tapers. *Opt. Express* **2010**, *18*, 22593–22598. [CrossRef] [PubMed]
80. Lai, K.; Leon-Saval, S.; Witkowska, A.; Wadsworth, W.; Birks, T. Wavelength-independent all-fiber mode converters. *Opt. Lett.* **2007**, *32*, 328–330. [CrossRef] [PubMed]
81. Yerolatsitis, S.; Gris-Sánchez, I.; Birks, T. Adiabatically-tapered fiber mode multiplexers. *Opt. Express* **2014**, *22*, 608–617. [CrossRef] [PubMed]
82. White, I.M.; Oveys, H.; Fan, X. Liquid-core optical ring-resonator sensors. *Opt. Lett.* **2006**, *31*, 1319–1321. [CrossRef] [PubMed]
83. Armani, A.M.; Vahala, K.J. Heavy water detection using ultra-high-Q microcavities. *Opt. Lett.* **2006**, *31*, 1896–1898. [CrossRef] [PubMed]
84. Keng, D.; McAnanama, S.; Teraoka, I.; Arnold, S. Resonance fluctuations of a whispering gallery mode biosensor by particles undergoing Brownian motion. *Appl. Phys. Lett.* **2007**, *91*, 103902. [CrossRef]
85. Socorro, A.B.; Del Villar, I.; Corres, J.M.; Arregui, F.J.; Matias, I.R. Tapered single-mode optical fiber pH sensor based on lossy mode resonances generated by a polymeric thin-film. *IEEE Sens. J.* **2012**, *12*, 2598–2603. [CrossRef]
86. Díaz-Herrera, N.; Navarrete, M.; Esteban, O.; González-Cano, A. A fibre-optic temperature sensor based on the deposition of a thermochromic material on an adiabatic taper. *Meas. Sci. Technol.* **2003**, *15*, 353. [CrossRef]
87. Esteban, Ó.; Díaz-Herrera, N.; Navarrete, M.-C.; González-Cano, A. Surface plasmon resonance sensors based on uniform-waist tapered fibers in a reflective configuration. *Appl. Opt.* **2006**, *45*, 7294–7298. [CrossRef] [PubMed]
88. Díaz-Herrera, N.; González-Cano, A.; Viegas, D.; Santos, J.L.; Navarrete, M.-C. Refractive index sensing of aqueous media based on plasmonic resonance in tapered optical fibres operating in the 1.5 µm region. *Sens. Actuators B Chem.* **2010**, *146*, 195–198. [CrossRef]
89. Lee, C.-L. Spectral analysis of waveguide tapered microfiber with an ultrathin metal coating. *Opt. Express* **2010**, *18*, 14768–14777. [CrossRef] [PubMed]

90. Herrera, N.D.; Esteban, Ó.; Navarrete, M.-C.; González-Cano, A.; Benito-Peña, E.; Orellana, G. Improved performance of SPR sensors by a chemical etching of tapered optical fibers. *Opt. Lasers Eng.* **2011**, *49*, 1065–1068. [CrossRef]
91. Kakarantzas, G.; Leon-Saval, S.; Birks, T.; Russell, P.S.J. Low-loss deposition of solgel-derived silica films on tapered fibers. *Opt. Lett.* **2004**, *29*, 694–696. [CrossRef] [PubMed]
92. Ab Razak, M.Z.; Reduan, S.A.; Sharbirin, A.S.; Jamaludin, N.; Zulkifli, M.Z.; Ahmad, H. Noncontact Optical Displacement Sensor Using an Adiabatic U-Shaped Tapered Fiber. *IEEE Sens. J.* **2015**, *15*, 5388–5392. [CrossRef]
93. Kieu, K.Q.; Mansuripur, M. Biconical fiber taper sensors. *IEEE Photonics Technol. Lett.* **2006**, *18*, 2239. [CrossRef]
94. Arregui, F.J.; Matías, I.R.; López-Amo, M. Optical fiber strain gauge based on a tapered single-mode fiber. *Sens. Actuators A Phys.* **2000**, *79*, 90–96. [CrossRef]
95. Mas, S.; Martí, J.; Monzón-Hernández, D.; Palací, J. Low-cost refractive index and strain sensor based on tapered fibers. *Opt. Commun.* **2016**, *361*, 99–103. [CrossRef]
96. Xu, L.; Li, Y.; Li, B. Nonadiabatic fiber taper-based Mach-Zehnder interferometer for refractive index sensing. *Appl. Phys. Lett.* **2012**, *101*, 153510. [CrossRef]
97. Ji, W.B.; Tan, Y.C.; Lin, B.; Tjin, S.C.; Chow, K.K. Nonadiabatically Tapered Microfiber Sensor with Ultrashort Waist. *IEEE Photonics Technol. Lett.* **2014**, *26*, 2303–2306. [CrossRef]
98. Muhammad, M.; Jasim, A.; Ahmad, H.; Arof, H.; Harun, S. Non-adiabatic silica microfiber for strain and temperature sensors. *Sens. Actuators A Phys.* **2013**, *192*, 130–132. [CrossRef]
99. Layeghi, A.; Latifi, H.; Frazao, O. Magnetic field sensor based on nonadiabatic tapered optical fiber with magnetic fluid. *IEEE Photonics Technol. Lett.* **2014**, *26*, 1904–1907. [CrossRef]
100. Zheng, Y.; Dong, X.; Chan, C.C.; Shum, P.P.; Su, H. Optical fiber magnetic field sensor based on magnetic fluid and microfiber mode interferometer. *Opt. Commun.* **2015**, *336*, 5–8. [CrossRef]
101. Liu, Z.J.; Yu, Y.S.; Zhang, X.Y.; Chen, C.; Zhu, C.C.; Meng, A.H.; Jing, S.M.; Sun, H.B. An optical microfiber taper magnetic field sensor with temperature compensation. *IEEE Sens. J.* **2015**, *15*, 4853–4856. [CrossRef]
102. Yu, Z.; Jin, L.; Sun, L.; Li, J.; Ran, Y.; Guan, B.-O. Highly Sensitive Fiber Taper Interferometric Hydrogen Sensors. *IEEE Photonics J.* **2016**, *8*, 1–9. [CrossRef]
103. Li, Y.; Wang, X.; Bao, X. Sensitive acoustic vibration sensor using single-mode fiber tapers. *Appl. Opt.* **2011**, *50*, 1873–1878.
104. Lu, P.; Harris, J.; Wang, X.; Lin, G.; Chen, L.; Bao, X. Tapered-fiber-based refractive index sensor at an air/solution interface. *Appl. Opt.* **2012**, *51*, 7368–7373. [CrossRef] [PubMed]
105. Wang, X.; Li, W.; Chen, L.; Bao, X. Thermal and mechanical properties of tapered single mode fiber measured by OFDR and its application for high-sensitivity force measurement. *Opt. Express* **2012**, *20*, 14779–14788. [CrossRef] [PubMed]
106. Lu, P.; Song, J.; Niedermayer, G.; Harris, J.; Chen, L.; Bao, X. Tapered polarization-maintaining fiber sensor based on analysis of polarization evolution. In Proceedings of the SPIE 9157, OFS2014 23rd International Conference on Optical Fiber Sensors, Santander, Spain, 2–6 June 2014.
107. Kumar, A.; Subrahmanyam, T.; Sharma, A.; Thyagarajan, K.; Pal, B.; Goyal, I. Novel refractometer using a tapered optical fibre. *Electron. Lett.* **1984**, *13*, 534–535. [CrossRef]
108. Villatoro, J.; Monzón-Hernández, D.; Talavera, D. High resolution refractive index sensing with cladded multimode tapered optical fibre. *Electron. Lett* **2004**, *40*, 106–107. [CrossRef]
109. Wang, P.; Brambilla, G.; Ding, M.; Semenova, Y.; Wu, Q.; Farrell, G. High-sensitivity, evanescent field refractometric sensor based on a tapered, multimode fiber interference. *Opt. Lett.* **2011**, *36*, 2233–2235. [CrossRef] [PubMed]
110. Biazoli, C.R.; Silva, S.; Franco, M.A.; Frazão, O.; Cordeiro, C.M. Multimode interference tapered fiber refractive index sensors. *Appl. Opt.* **2012**, *51*, 5941–5945. [CrossRef] [PubMed]
111. Luo, H.; Sun, Q.; Xu, Z.; Liu, D.; Zhang, L. Simultaneous measurement of refractive index and temperature using multimode microfiber-based dual Mach-Zehnder interferometer. *Opt. Lett.* **2014**, *39*, 4049–4052. [CrossRef] [PubMed]
112. Mägi, E.; Steinvurzel, P.; Eggleton, B. Tapered photonic crystal fibers. *Opt. Express* **2004**, *12*, 776–784. [CrossRef] [PubMed]

113. Nguyen, H.C.; Kuhlmey, B.T.; Mägi, E.C.; Steel, M.J.; Domachuk, P.; Smith, C.L.; Eggleton, B.J. Tapered photonic crystal fibres: Properties, characterisation and applications. *Appl. Phys. B* **2005**, *81*, 377–387. [CrossRef]
114. Minkovich, V.; Villatoro, J.; Monzón-Hernández, D.; Calixto, S.; Sotsky, A.; Sotskaya, L. Holey fiber tapers with resonance transmission for high-resolution refractive index sensing. *Opt. Express* **2005**, *13*, 7609–7614. [CrossRef] [PubMed]
115. Villatoro, J.; Minkovich, V.P.; Monzón-Hernández, D. Compact modal interferometer built with tapered microstructured optical fiber. *IEEE Photonics Technol. Lett.* **2006**, *18*, 1258–1260. [CrossRef]
116. Villatoro, J.; Finazzi, V.; Badenes, G.; Pruneri, V. Highly sensitive sensors based on photonic crystal fiber modal interferometers. *J. Sens.* **2009**, *2009*, 747803. [CrossRef]
117. Pinto, A.M.; Lopez-Amo, M. Photonic crystal fibers for sensing applications. *J. Sens.* **2012**, *2012*, 598178. [CrossRef]
118. Monzón-Hernández, D.; Minkovich, V.P.; Villatoro, J. High-temperature sensing with tapers made of microstructured optical fiber. *IEEE Photonics Technol. Lett.* **2006**, *18*, 511–513. [CrossRef]
119. Villatoro, J.; Minkovich, V.P.; Monzón-Hernández, D. Temperature-independent strain sensor made from tapered holey optical fiber. *Opt. Lett.* **2006**, *31*, 305–307. [CrossRef] [PubMed]
120. Qiu, S.-J.; Chen, Y.; Kou, J.-L.; Xu, F.; Lu, Y.-Q. Miniature tapered photonic crystal fiber interferometer with enhanced sensitivity by acid microdroplets etching. *Appl. Opt.* **2011**, *50*, 4328–4332. [CrossRef] [PubMed]
121. Ni, K.; Li, T.; Hu, L.; Qian, W.; Zhang, Q.; Jin, S. Temperature-independent curvature sensor based on tapered photonic crystal fiber interferometer. *Opt. Commun.* **2012**, *285*, 5148–5150. [CrossRef]
122. Ni, K.; Chan, C.C.; Dong, X.; Poh, C.; Li, T. Temperature-independent refractometer based on a tapered photonic crystal fiber interferometer. *Opt. Commun.* **2013**, *291*, 238–241. [CrossRef]
123. Li, C.; Qiu, S.-J.; Chen, Y.; Xu, F.; Lu, Y.-Q. Ultra-sensitive refractive index sensor with slightly tapered photonic crystal fiber. *IEEE Photonics Technol. Lett.* **2012**, *24*, 1771. [CrossRef]
124. Zhao, Y.; Wu, D.; Lv, R.-Q. Magnetic field sensor based on photonic crystal fiber taper coated with ferrofluid. *IEEE Photonics Technol. Lett.* **2015**, *27*, 26–29. [CrossRef]
125. Wu, Q.; Semenova, Y.; Wang, P.; Farrell, G. A comprehensive analysis verified by experiment of a refractometer based on an SMF28–small-core singlemode fiber (SCSMF)-SMF28 fiber structure. *J. Opt.* **2011**, *13*, 125401. [CrossRef]
126. Liu, D.; Mallik, A.K.; Yuan, J.; Yu, C.; Farrell, G.; Semenova, Y.; Wu, Q. High sensitivity refractive index sensor based on a tapered small core single-mode fiber structure. *Opt. Lett.* **2015**, *40*, 4166–4169. [CrossRef] [PubMed]
127. Wu, X.; Tong, L. Optical microfibers and nanofibers. *Nanophotonics* **2013**, *2*, 407–428. [CrossRef]
128. Sumetsky, M.; Dulashko, Y.; Fini, J.; Hale, A.; DiGiovanni, D. The microfiber loop resonator: Theory, experiment, and application. *J. Lightwave Technol.* **2006**, *24*, 242. [CrossRef]
129. Jung, Y.; Murugan, G.S.; Brambilla, G.; Richardson, D.J. Embedded Optical Microfiber Coil Resonator with Enhanced High. *IEEE Photonics Technol. Lett.* **2010**, *22*, 1638–1640.
130. Bueno, F.-J.; Esteban, O.; Díaz-Herrera, N.; Navarrete, M.-C.; González-Cano, A. Sensing properties of asymmetric double-layer-covered tapered fibers. *Appl. Opt.* **2004**, *43*, 1615–1620. [CrossRef] [PubMed]
131. Caspar, C.; Bachus, E.-J. Fibre-optic micro-ring-resonator with 2 mm diameter. *Electron. Lett.* **1989**, *25*, 1506–1508. [CrossRef]
132. Sumetsky, M.; Dulashko, Y.; Fini, J.M.; Hale, A. Optical microfiber loop resonator. *Appl. Phys. Lett.* **2005**, *86*, 161108. [CrossRef]
133. Guo, X.; Li, Y.; Jiang, X.; Tong, L. Demonstration of critical coupling in microfiber loops wrapped around a copper rod. *Appl. Phys. Lett.* **2007**, *91*, 073512. [CrossRef]
134. Guo, X.; Tong, L. Supported microfiber loops for optical sensing. *Opt. Express* **2008**, *16*, 14429–14434. [CrossRef] [PubMed]
135. Pal, P.; Knox, W.H. Fabrication and characterization of fused microfiber resonators. *IEEE Photonics Technol. Lett.* **2009**, *12*, 766–768. [CrossRef]
136. Wang, P.; Zhang, L.; Yang, Z.; Gu, F.; Wang, S.; Yang, Q.; Tong, L. Fusion spliced microfiber closed-loop resonators. *IEEE Photonics Technol. Lett.* **2010**, *15*, 1075–1077. [CrossRef]
137. Wang, S.; Wang, J.; Li, G.; Tong, L. Modeling optical microfiber loops for seawater sensing. *Appl. Opt.* **2012**, *51*, 3017–3023. [CrossRef] [PubMed]

138. Zheng, Y.; Dong, X.; Zhao, C.; Li, Y.; Shao, L.; Jin, S. Relative humidity sensor based on microfiber loop resonator. *Adv. Mater. Sci. Eng.* **2013**, *2013*, 815930. [CrossRef]
139. Yoon, M.-S.; Kim, S.K.; Han, Y.-G. Highly sensitive current sensor based on an optical microfiber loop resonator incorporating low index polymer overlay. *J. Lightwave Technol.* **2015**, *33*, 2386–2391. [CrossRef]
140. Wang, Y.; Zhu, H.; Li, B. Optical characterization of mechanically tunable microwire based resonators by changing ring radius and wire diameter. *Opt. Commun.* **2011**, *284*, 3276–3279. [CrossRef]
141. Chen, Z.; Hsiao, V.K.; Li, X.; Li, Z.; Yu, J.; Zhang, J. Optically tunable microfiber-knot resonator. *Opt. Express* **2011**, *19*, 14217–14222. [CrossRef] [PubMed]
142. Tong, L.; Gattass, R.R.; Ashcom, J.B.; He, S.; Lou, J.; Shen, M.; Maxwell, I.; Mazur, E. Subwavelength-diameter silica wires for low-loss optical wave guiding. *Nature* **2003**, *426*, 816–819. [CrossRef] [PubMed]
143. Jiang, X.; Tong, L.; Vienne, G.; Guo, X.; Tsao, A.; Yang, Q.; Yang, D. Demonstration of optical microfiber knot resonators. *Appl. Phys. Lett.* **2006**, *88*, 223501. [CrossRef]
144. Vienne, G.; Li, Y.; Tong, L. Effect of host polymer on microfiber resonator. *IEEE Photonics Technol. Lett.* **2007**, *19*, 1386–1388. [CrossRef]
145. Zeng, X.; Wu, Y.; Hou, C.; Bai, J.; Yang, G. A temperature sensor based on optical microfiber knot resonator. *Opt. Commun.* **2009**, *282*, 3817–3819. [CrossRef]
146. Wu, Y.; Rao, Y.-J.; Chen, Y.-H.; Gong, Y. Miniature fiber-optic temperature sensors based on silica/polymer microfiber knot resonators. *Opt. Express* **2009**, *17*, 18142–18147. [CrossRef] [PubMed]
147. Wu, Y.; Zhang, T.; Rao, Y.; Gong, Y. Miniature interferometric humidity sensors based on silica/polymer microfiber knot resonators. *Sens. Actuators B Chem.* **2011**, *155*, 258–263. [CrossRef]
148. Li, X.; Ding, H. Investigation of the thermal properties of optical microfiber knot resonators. *Instrum. Sci. Technol.* **2013**, *41*, 224–235. [CrossRef]
149. Lim, K.; Harun, S.; Damanhuri, S.; Jasim, A.; Tio, C.; Ahmad, H. Current sensor based on microfiber knot resonator. *Sens. Actuators A Phys.* **2011**, *167*, 60–62. [CrossRef]
150. Li, X.; Ding, H. All-fiber magnetic-field sensor based on microfiber knot resonator and magnetic fluid. *Opt. Lett.* **2012**, *37*, 5187–5189. [CrossRef]
151. Lim, K.-S.; Aryanfar, I.; Chong, W.-Y.; Cheong, Y.-K.; Harun, S.W.; Ahmad, H. Integrated microfibre device for refractive index and temperature sensing. *Sensors* **2012**, *12*, 11782–11789. [CrossRef]
152. Li, X.; Ding, H. A stable evanescent field-based microfiber knot resonator refractive index sensor. *IEEE Photonics Technol. Lett.* **2014**, *26*, 1625–1628. [CrossRef]
153. Gomes, A.D.; Frazão, O. Mach-Zehnder Based on Large Knot Fiber Resonator for Refractive Index Measurement. *IEEE Photonics Technol. Lett.* **2016**, *28*, 1279–1281. [CrossRef]
154. Larocque, H.; Lu, P.; Bao, X. Phase-shift detection in a Fourier-transform method for temperature sensing using a tapered fiber microknot resonator. *Opt. Lett.* **2016**, *41*, 1344–1347. [CrossRef] [PubMed]
155. Sulaiman, A.; Harun, S.; Ahmad, F.; Muhammad, M.Z.; Jasim, A.A.; Ahmad, H. Demonstration of microfiber hybrid Mach–Zehnder and knot resonator structure. *Microw. Opt. Technol. Lett.* **2013**, *55*, 100–102. [CrossRef]
156. Sun, L.; Li, J.; Tan, Y.; Shen, X.; Xie, X.; Gao, S.; Guan, B.-O. Miniature highly-birefringent microfiber loop with extremely-high refractive index sensitivity. *Opt. Express* **2012**, *20*, 10180–10185. [CrossRef] [PubMed]
157. Wu, Y.; Jia, L.; Zhang, T.; Rao, Y.; Gong, Y. Microscopic multi-point temperature sensing based on microfiber double-knot resonators. *Opt. Commun.* **2012**, *285*, 2218–2222. [CrossRef]
158. Xu, Z.; Sun, Q.; Li, B.; Luo, Y.; Lu, W.; Liu, D.; Shum, P.P.; Zhang, L. Highly sensitive refractive index sensor based on cascaded microfiber knots with Vernier effect. *Opt. Express* **2015**, *23*, 6662–6672. [CrossRef] [PubMed]
159. Shahal, S.; Klein, A.; Masri, G.; Fridman, M. Fused fiber micro-knots. *Appl. Opt.* **2016**, *55*, 4538–4541. [CrossRef] [PubMed]
160. Sumetsky, M. Basic elements for microfiber photonics: Micro/nanofibers and microfiber coil resonators. *J. Lightwave Technol.* **2008**, *26*, 21–27. [CrossRef]
161. Scheuer, J.; Sumetsky, M. Optical-fiber microcoil waveguides and resonators and their applications for interferometry and sensing. *Laser Photonics Rev.* **2011**, *5*, 465–478. [CrossRef]
162. Sumetsky, M. Optical fiber microcoil resonators. *Opt. Express* **2004**, *12*, 2303–2316. [CrossRef] [PubMed]
163. Xu, F.; Horak, P.; Brambilla, G. Conical and biconical ultra-high-Q optical-fiber nanowire microcoil resonator. *Appl. Opt.* **2007**, *46*, 570–573. [CrossRef] [PubMed]

164. Xu, F.; Brambilla, G.; Feng, J.; Lu, Y. Mathematical model for manufacturing microfiber coil resonators. *Opt. Eng.* **2010**, *49*, 044001.
165. Xu, F.; Wang, Q.; Zhou, J.-F.; Hu, W.; Lu, Y.-Q. Dispersion study of optical nanowire microcoil resonators. *IEEE J. Sel. Top. Quantum Electron.* **2011**, *17*, 1102–1106. [CrossRef]
166. Xu, F.; Brambilla, G. Manufacture of 3-D microfiber coil resonators. *IEEE Photonics Technol. Lett.* **2007**, *19*, 1481–1483. [CrossRef]
167. Xu, F.; Brambilla, G. Embedding optical microfiber coil resonators in Teflon. *Opt. Lett.* **2007**, *32*, 2164–2166. [CrossRef] [PubMed]
168. Xu, F.; Horak, P.; Brambilla, G. Optical microfiber coil resonator refractometric sensor. *Opt. Express* **2007**, *15*, 7888–7893. [CrossRef] [PubMed]
169. Xu, F.; Brambilla, G. Demonstration of a refractometric sensor based on optical microfiber coil resonator. *Appl. Phys. Lett.* **2008**, *92*, 101126. [CrossRef]
170. Scheuer, J. Fiber microcoil optical gyroscope. *Opt. Lett.* **2009**, *34*, 1630–1632. [CrossRef] [PubMed]
171. Lorenzi, R.; Jung, Y.; Brambilla, G. In-line absorption sensor based on coiled optical microfiber. *Appl. Phys. Lett.* **2011**, *98*, 173504. [CrossRef]
172. Hsieh, Y.-C.; Peng, T.-S.; Wang, L.A. Millimeter-sized microfiber coil resonators with enhanced quality factors by increasing coil numbers. *IEEE Photonics Technol. Lett.* **2012**, *24*, 569–571.
173. Chen, G.Y.; Brambilla, G.; Newson, T.P. Compact acoustic sensor based on air-backed mandrel coiled with optical microfiber. *Opt. Lett.* **2012**, *37*, 4720–4722. [CrossRef] [PubMed]
174. Chen, G.; Brambilla, G.; Newson, T. Inspection of electrical wires for insulation faults and current surges using sliding temperature sensor based on optical Microfibre coil resonator. *Electron. Lett.* **2013**, *49*, 46–47. [CrossRef]
175. Xie, X.; Li, J.; Sun, L.-P.; Shen, X.; Jin, L.; Guan, B.-O. A High-Sensitivity Current Sensor Utilizing CrNi Wire and Microfiber Coils. *Sensors* **2014**, *14*, 8423–8429. [CrossRef] [PubMed]
176. Kou, J.-L.; Chen, J.-H.; Chen, Y.; Xu, F.; Lu, Y.-Q. Platform for enhanced light–graphene interaction length and miniaturizing fiber stereo devices. *Optica* **2014**, *1*, 307–310. [CrossRef]
177. Yan, S.-C.; Zheng, B.-C.; Chen, J.-H.; Xu, F.; Lu, Y.-Q. Optical electrical current sensor utilizing a graphene-microfiber-integrated coil resonator. *Appl. Phys. Lett.* **2015**, *107*, 053502. [CrossRef]
178. Coelho, J.M.; Nespereira, M.; Silva, C.; Pereira, D.; Rebordão, J. Advances in Optical Fiber Laser Micromachining for Sensors Development. *Curr. Dev. Opt. Fiber Technol.* **2013**, 375–401.
179. Van Brakel, A.; Grivas, C.; Petrovich, M.N.; Richardson, D.J. Micro-channels machined in microstructured optical fibers by femtosecond laser. *Opt. Express* **2007**, *15*, 8731–8736. [CrossRef] [PubMed]
180. Konstantaki, M.; Childs, P.; Sozzi, M.; Pissadakis, S. Relief Bragg reflectors inscribed on the capillary walls of solid-core photonic crystal fibers. *Laser Photonics Rev.* **2013**, *7*, 439–443. [CrossRef]
181. Davis, K.M.; Miura, K.; Sugimoto, N.; Hirao, K. Writing waveguides in glass with a femtosecond laser. *Opt. Lett.* **1996**, *21*, 1729–1731. [CrossRef] [PubMed]
182. Martinez, A.; Dubov, M.; Khrushchev, I.; Bennion, I. Direct writing of fibre Bragg gratings by femtosecond laser. *Electron. Lett.* **2004**, *40*, 1. [CrossRef]
183. Streltsov, A.M.; Borrelli, N.F. Fabrication and analysis of a directional coupler written in glass by nanojoule femtosecond laser pulses. *Opt. Lett.* **2001**, *26*, 42–43. [CrossRef] [PubMed]
184. Wang, Y.; Li, Y.; Liao, C.; Wang, D.; Yang, M.; Lu, P. High-temperature sensing using miniaturized fiber in-line Mach–Zehnder interferometer. *IEEE Photonics Technol. Lett.* **2010**, *22*, 39–41. [CrossRef]
185. Jiang, L.; Yang, J.; Wang, S.; Li, B.; Wang, M. Fiber Mach-Zehnder interferometer based on microcavities for high-temperature sensing with high sensitivity. *Opt. Lett.* **2011**, *36*, 3753–3755. [CrossRef] [PubMed]
186. Cao, Z.; Jiang, L.; Wang, S.; Wang, P.; Zhang, F.; Lu, Y. Trench-embedding fiber taper sensor fabricated by a femtosecond laser for gas refractive index sensing. *Appl. Opt.* **2014**, *53*, 1028–1032. [CrossRef] [PubMed]
187. Rao, Y.-J.; Deng, M.; Duan, D.-W.; Yang, X.-C.; Zhu, T.; Cheng, G.-H. Micro Fabry-Perot interferometers in silica fibers machined by femtosecond laser. *Opt. Express* **2007**, *15*, 14123–14128. [CrossRef] [PubMed]
188. Wei, T.; Han, Y.; Li, Y.; Tsai, H.-L.; Xiao, H. Temperature-insensitive miniaturized fiber inline Fabry-Perot interferometer for highly sensitive refractive index measurement. *Opt. Express* **2008**, *16*, 5764–5769. [CrossRef] [PubMed]
189. Wei, T.; Han, Y.; Tsai, H.-L.; Xiao, H. Miniaturized fiber inline Fabry-Perot interferometer fabricated with a femtosecond laser. *Opt. Lett.* **2008**, *33*, 536–538. [CrossRef] [PubMed]

190. Wang, Y.; Wang, D.; Yang, M.; Hong, W.; Lu, P. Refractive index sensor based on a microhole in single-mode fiber created by the use of femtosecond laser micromachining. *Opt. Lett.* **2009**, *34*, 3328–3330. [CrossRef] [PubMed]
191. Liao, C.; Hu, T.; Wang, D. Optical fiber Fabry-Perot interferometer cavity fabricated by femtosecond laser micromachining and fusion splicing for refractive index sensing. *Opt. Express* **2012**, *20*, 22813–22818.
192. Liu, Y.; Qu, S.; Li, Y. Single microchannel high-temperature fiber sensor by femtosecond laser-induced water breakdown. *Opt. Lett.* **2013**, *38*, 335–337. [CrossRef] [PubMed]
193. Ran, Z.; Rao, Y.; Deng, H.; Liao, X. Miniature in-line photonic crystal fiber etalon fabricated by 157 nm laser micromachining. *Opt. Lett.* **2007**, *32*, 3071–3073. [CrossRef] [PubMed]
194. Ran, Z.L.; Rao, Y.J.; Liu, W.J.; Liao, X.; Chiang, K.S. Laser-micromachined Fabry-Perot optical fiber tip sensor for high-resolution temperature-independent measurement of refractive index. *Opt. Express* **2008**, *16*, 2252–2263. [CrossRef] [PubMed]
195. Ran, Z.; Liu, Z.; Rao, Y.; Xu, F.; Sun, D.; Yu, X.; Xu, B.; Zhang, J. Miniature fiber-optic tip high pressure sensors micromachined by 157 nm laser. *IEEE Sens. J.* **2011**, *11*, 1103–1106. [CrossRef]
196. Ran, Z.; Li, C.; Zuo, H.; Chen, Y. Laser-machined cascaded micro cavities for simultaneous measurement of dual parameters under high temperature. *IEEE Sens. J.* **2013**, *13*, 1988–1991. [CrossRef]
197. Tai, Y.-H.; Wei, P.-K. Sensitive liquid refractive index sensors using tapered optical fiber tips. *Opt. Lett.* **2010**, *35*, 944–946. [CrossRef] [PubMed]
198. Donlagic, D. All-fiber micromachined microcell. *Opt. Lett.* **2011**, *36*, 3148–3150. [CrossRef] [PubMed]
199. Pevec, S.; Donlagic, D. Miniature micro-wire based optical fiber-field access device. *Opt. Express* **2012**, *20*, 27874–27887. [CrossRef] [PubMed]
200. Pevec, S.; Donlagic, D. Miniature fiber-optic sensor for simultaneous measurement of pressure and refractive index. *Opt. Lett.* **2014**, *39*, 6221–6224. [CrossRef] [PubMed]
201. Pevec, S.; Donlagic, D. Miniature all-silica fiber-optic sensor for simultaneous measurement of relative humidity and temperature. *Opt. Lett.* **2015**, *40*, 5646–5649. [CrossRef] [PubMed]
202. Tafulo, P.A.; Jorge, P.A.; Santos, J.L.; Araujo, F.M.; Frazao, O. Intrinsic Fabry-Pérot cavity sensor based on etched multimode graded index fiber for strain and temperature measurement. *IEEE Sens. J.* **2012**, *12*, 8–12. [CrossRef]
203. Erreira, M.S.; Bierlich, J.; Unger, S.; Schuster, K.; Santos, J.L.; Frazão, O. Post-processing of Fabry-Pérot microcavity tip sensor. *IEEE Photonics Technol. Lett.* **2013**, *25*, 1593–1596. [CrossRef]
204. Pevec, S.; Donlagic, D. High resolution, all-fiber, micro-machined sensor for simultaneous measurement of refractive index and temperature. *Opt. Express* **2014**, *22*, 16241–16253. [CrossRef] [PubMed]
205. Wu, S.; Yan, G.; Zhou, B.; Lee, E.-H.; He, S. Open-cavity fabry-perot interferometer based on etched side-hole fiber for microfluidic sensing. *IEEE Photonics Technol. Lett.* **2015**, *27*, 1813–1816.
206. Lu, P.; Xu, Y.; Baset, F.; Bao, X.; Bhardwaj, R. In-line fiber microcantilever vibration sensor. *Appl. Phys. Lett.* **2013**, *103*, 211113. [CrossRef]
207. André, R.M.; Warren-Smith, S.C.; Becker, M.; Dellith, J.; Rothhardt, M.; Zibaii, M.; Latifi, H.; Marques, M.B.; Bartelt, H.; Frazão, O. Simultaneous measurement of temperature and refractive index using focused ion beam milled Fabry-Perot cavities in optical fiber micro-tips. *Opt. Express* **2016**, *24*, 14053–14065. [CrossRef]
208. Kou, J.-L.; Feng, J.; Ye, L.; Xu, F.; Lu, Y.-Q. Miniaturized fiber taper reflective interferometer for high temperature measurement. *Opt. Express* **2010**, *18*, 14245–14250. [CrossRef] [PubMed]
209. Kou, J.-L.; Feng, J.; Wang, Q.-J.; Xu, F.; Lu, Y.-Q. Microfiber-probe-based ultrasmall interferometric sensor. *Opt. Lett.* **2010**, *35*, 2308–2310. [CrossRef] [PubMed]
210. André, R.M.; Pevec, S.; Becker, M.; Dellith, J.; Rothhardt, M.; Marques, M.B.; Donlagic, D.; Bartelt, H.; Frazão, O. Focused ion beam post-processing of optical fiber Fabry-Perot cavities for sensing applications. *Opt. Express* **2014**, *22*, 13102–13108. [CrossRef] [PubMed]
211. Wieduwilt, T.; Dellith, J.; Talkenberg, F.; Bartelt, H.; Schmidt, M. Reflectivity enhanced refractive index sensor based on a fiber-integrated Fabry-Perot microresonator. *Opt. Express* **2014**, *22*, 25333–25346. [CrossRef] [PubMed]
212. Li, X.; Shao, Y.; Yu, Y.; Zhang, Y.; Wei, S. A Highly Sensitive Fiber-Optic Fabry-Perot Interferometer Based on Internal Reflection Mirrors for Refractive Index Measurement. *Sensors* **2016**, *16*, 794. [CrossRef] [PubMed]
213. Juan, M.L.; Gordon, R.; Pang, Y.; Eftekhari, F.; Quidant, R. Self-induced back-action optical trapping of dielectric nanoparticles. *Nat. Phys.* **2009**, *5*, 915–919.

214. Berthelot, J.; Aćimović, S.; Juan, M.; Kreuzer, M.; Renger, J.; Quidant, R. Three-dimensional manipulation with scanning near-field optical nanotweezers. *Nat. Nanotechnol.* **2014**, *9*, 295–299. [CrossRef] [PubMed]
215. El Eter, A.; Hameed, N.M.; Baida, F.I.; Salut, R.; Filiatre, C.; Nedeljkovic, D.; Atie, E.; Bole, S.; Grosjean, T. Fiber-integrated optical nano-tweezer based on a bowtie-aperture nano-antenna at the apex of a SNOM tip. *Opt. Express* **2014**, *22*, 10072–10080. [CrossRef] [PubMed]
216. Hameed, N.M.; El Eter, A.; Grosjean, T.; Baida, F.I. Stand-alone three-dimensional optical tweezers based on fibred Bowtie nanoaperture. *IEEE Photonics J.* **2014**, *6*, 1–10. [CrossRef]
217. Atie, E.M.; Xie, Z.; El Eter, A.; Salut, R.; Nedeljkovic, D.; Tannous, T.; Baida, F.I.; Grosjean, T. Remote optical sensing on the nanometer scale with a bowtie aperture nano-antenna on a fiber tip of scanning near-field optical microscopy. *Appl. Phys. Lett.* **2015**, *106*, 151104. [CrossRef]
218. Gelfand, R.M.; Wheaton, S.; Gordon, R. Cleaved fiber optic double nanohole optical tweezers for trapping nanoparticles. *Opt. Lett.* **2014**, *39*, 6415–6417. [CrossRef] [PubMed]
219. Gong, Y.; Guo, Y.; Rao, Y.-J.; Zhao, T.; Wu, Y. Fiber-optic Fabry-Perot sensor based on periodic focusing effect of graded-index multimode fibers. *IEEE Photonics Technol. Lett.* **2010**, *22*, 1708–1710. [CrossRef]
220. Wang, T.; Wang, M. Fabry-Pérot fiber sensor for simultaneous measurement of refractive index and temperature based on an In-Fiber Ellipsoidal Cavity. *IEEE Photonics Technol. Lett.* **2012**, *24*, 1733–1736. [CrossRef]
221. Wu, C.; Liu, Z.; Zhang, A.P.; Guan, B.-O.; Tam, H.-Y. In-line open-cavity Fabry–Pérot interferometer formed by C-shaped fiber fortemperature-insensitive refractive index sensing. *Opt. Express* **2014**, *22*, 21757–21766. [CrossRef] [PubMed]
222. Jauregui-Vazquez, D.; Estudillo-Ayala, J.; Castillo-Guzman, A.; Rojas-Laguna, R.; Selvas-Aguilar, R.; Vargas-Rodriguez, E.; Sierra-Hernandez, J.; Guzman-Ramos, V.; Flores-Balderas, A. Highly sensitive curvature and displacement sensing setup based on an all fiber micro Fabry-Perot interferometer. *Opt. Commun.* **2013**, *308*, 289–292. [CrossRef]
223. Jauregui-Vazquez, D.; Lopez-Dieguez, Y.; Sierra-Hernandez, J.; Perez-Maciel, M.; Avila-Garcia, M.; Vargas-Rodriguez, E.; Rojas-Laguna, R.; Estudillo-Ayala, J. Modified All-Fiber Fabry-Perot Interferometer and Its Refractive Index, Load, and Temperature Analyses. *IEEE Photonics J.* **2015**, *7*, 1–9. [CrossRef]
224. Lee, C.-L.; Hsu, J.-M.; Horng, J.-S.; Sung, W.-Y.; Li, C.-M. Microcavity fiber Fabry–Pérot interferometer with an embedded golden thin film. *IEEE Photonics Technol. Lett.* **2013**, *25*, 833–836. [CrossRef]
225. Gruca, G.; Chavan, D.; Rector, J.; Heeck, K.; Iannuzzi, D. Demonstration of an optically actuated ferrule-top device for pressure and humidity sensing. *Sens. Actuators A Phys.* **2013**, *190*, 77–83. [CrossRef]
226. Williams, H.E.; Freppon, D.J.; Kuebler, S.M.; Rumpf, R.C.; Melino, M.A. Fabrication of three-dimensional micro-photonic structures on the tip of optical fibers using SU-8. *Opt. Express* **2011**, *19*, 22910–22922. [CrossRef] [PubMed]
227. Melissinaki, V.; Farsari, M.; Pissadakis, S. A Fiber-Endface, Fabry-Perot Vapor Microsensor Fabricated by Multiphoton Polymerization. *IEEE J. Sel. Top. Quantum Electron.* **2015**, *21*, 344–353. [CrossRef]
228. Liang, W.; Huang, Y.; Xu, Y.; Lee, R.K.; Yariv, A. Highly sensitive fiber Bragg grating refractive index sensors. *Appl. Phys. Lett.* **2005**, *86*, 151122. [CrossRef]
229. Zhang, Y.; Lin, B.; Tjin, S.C.; Zhang, H.; Wang, G.; Shum, P.; Zhang, X. Refractive index sensing based on higher-order mode reflection of a microfiber Bragg grating. *Opt. Express* **2010**, *18*, 26345–26350.
230. Ran, Y.; Tan, Y.-N.; Sun, L.-P.; Gao, S.; Li, J.; Jin, L.; Guan, B.-O. 193 nm excimer laser inscribed Bragg gratings in microfibers for refractive index sensing. *Opt. Express* **2011**, *19*, 18577–18583. [CrossRef] [PubMed]
231. Chung, K.M.; Liu, Z.; Lu, C.; Tam, H.-Y. Highly sensitive compact force sensor based on microfiber Bragg grating. *IEEE Photonics Technol. Lett.* **2012**, *24*, 700–702. [CrossRef]
232. Ran, Y.; Jin, L.; Tan, Y.-N.; Sun, L.-P.; Li, J.; Guan, B.-O. High-efficiency ultraviolet inscription of Bragg gratings in microfibers. *IEEE Photonics J.* **2012**, *4*, 181–186. [CrossRef]
233. Ran, Y.; Jin, L.; Sun, L.-P.; Li, J.; Guan, B.-O. Temperature-compensated refractive-index sensing using a single Bragg grating in an abrupt fiber taper. *IEEE Photonics J.* **2013**, *5*, 7100208.
234. Yu, Z.; Jin, L.; Chen, L.; Li, J.; Ran, Y.; Guan, B.-O. Microfiber Bragg grating hydrogen sensors. *IEEE Photonics Technol. Lett.* **2015**, *27*, 2575–2578. [CrossRef]
235. Mihailov, S.J.; Smelser, C.W.; Lu, P.; Walker, R.B.; Grobnic, D.; Ding, H.; Henderson, G.; Unruh, J. Fiber Bragg gratings made with a phase mask and 800-nm femtosecond radiation. *Opt. Lett.* **2003**, *28*, 995–997. [CrossRef]

236. Grobnic, D.; Mihailov, S.J.; Ding, H.; Smelser, C.W. Bragg grating evanescent field sensor made in biconical tapered fiber with femtosecond IR radiation. *IEEE Photonics Technol. Lett.* **2006**, *18*, 160–162. [CrossRef]
237. Fang, X.; Liao, C.; Wang, D. Femtosecond laser fabricated fiber Bragg grating in microfiber for refractive index sensing. *Opt. Lett.* **2010**, *35*, 1007–1009. [CrossRef] [PubMed]
238. Zhao, P.; Li, Y.; Zhang, J.; Shi, L.; Zhang, X. Nanohole induced microfiber Bragg gratings. *Opt. Express* **2012**, *20*, 28625–28630. [CrossRef]
239. Ahmed, F.; Ahsani, V.; Saad, A.; Jun, M.B. Bragg Grating Embedded in Mach-Zehnder Interferometer for Refractive Index and Temperature Sensing. *IEEE Photonics Technol. Lett.* **2016**, *28*, 1968–1971. [CrossRef]
240. Ahmed, F.; Jun, M.B. Microfiber Bragg Grating Sandwiched Between Standard Optical Fibers for Enhanced Temperature Sensing. *IEEE Photonics Technol. Lett.* **2016**, *28*, 685–688. [CrossRef]
241. Liu, Y.; Meng, C.; Zhang, A.P.; Xiao, Y.; Yu, H.; Tong, L. Compact microfiber Bragg gratings with high-index contrast. *Opt. Lett.* **2011**, *36*, 3115–3117. [CrossRef] [PubMed]
242. Kou, J.-L.; Qiu, S.-J.; Xu, F.; Lu, Y.-Q. Demonstration of a compact temperature sensor based on first-order Bragg grating in a tapered fiber probe. *Opt. Express* **2011**, *19*, 18452–18457.
243. Ding, M.; Zervas, M.N.; Brambilla, G. A compact broadband microfiber Bragg grating. *Opt. Express* **2011**, *19*, 15621–15626. [CrossRef] [PubMed]
244. Ahmad, R.; Rochette, M.; Baker, C. Fabrication of Bragg gratings in subwavelength diameter As_2Se_3 chalcogenide wires. *Opt. Lett.* **2011**, *36*, 2886–2888. [CrossRef] [PubMed]
245. Rajan, G.; Noor, M.Y.M.; Lovell, N.H.; Ambikaizrajah, E.; Farrell, G.; Peng, G.-D. Polymer micro-fiber Bragg grating. *Opt. Lett.* **2013**, *38*, 3359–3362. [CrossRef] [PubMed]
246. Yao, B.; Wu, Y.; Zhang, A.; Wang, F.; Rao, Y.; Gong, Y.; Zhang, W.; Wang, Z.; Chiang, K.; Sumetsky, M. Graphene Bragg gratings on microfiber. *Opt. Express* **2014**, *22*, 23829–23835. [CrossRef] [PubMed]
247. Wu, Y.; Yao, B.; Zhang, A.; Rao, Y.; Wang, Z.; Cheng, Y.; Gong, Y.; Zhang, W.; Chen, Y.; Chiang, K. Graphene-coated microfiber Bragg grating for high-sensitivity gas sensing. *Opt. Lett.* **2014**, *39*, 1235–1237. [CrossRef] [PubMed]
248. Allsop, T.; Floreani, F.; Jedrzejewski, K.; Marques, P.; Romero, R.; Webb, D.; Bennion, I. Refractive index sensing with long-period grating fabricated in biconical tapered fibre. *Electron. Lett.* **2005**, *41*, 1. [CrossRef]
249. Allsop, T.; Floreani, F.; Jedrzejewski, K.; Marques, P.; Romero, R.; Webb, D.J.; Bennion, I. Spectral characteristics of tapered LPG device as a sensing element for refractive index and temperature. *J. Lightwave Technol.* **2006**, *24*, 870. [CrossRef]
250. Xuan, H.; Jin, W.; Zhang, M. CO_2 laser induced long period gratings in optical microfibers. *Opt. Express* **2009**, *17*, 21882–21890. [CrossRef] [PubMed]
251. Xuan, H.; Jin, W.; Liu, S. Long-period gratings in wavelength-scale microfibers. *Opt. Lett.* **2010**, *35*, 85–87. [CrossRef] [PubMed]
252. Sun, L.-P.; Li, J.; Jin, L.; Guan, B.-O. Structural microfiber long-period gratings. *Opt. Express* **2012**, *20*, 18079–18084. [CrossRef] [PubMed]
253. Ji, W.B.; Tjin, S.C.; Lin, B.; Ng, C.L. Highly sensitive refractive index sensor based on adiabatically tapered microfiber long period gratings. *Sensors* **2013**, *13*, 14055–14063. [CrossRef] [PubMed]
254. Yoon, M.-S.; Kim, H.-J.; Kim, S.-J.; Han, Y.-G. Influence of the waist diameters on transmission characteristics and strain sensitivity of microtapered long-period fiber gratings. *Opt. Lett.* **2013**, *38*, 2669–2672. [CrossRef] [PubMed]
255. Tan, Y.; Sun, L.-P.; Jin, L.; Li, J.; Guan, B.-O. Microfiber Mach-Zehnder interferometer based on long period grating for sensing applications. *Opt. Express* **2013**, *21*, 154–164. [CrossRef] [PubMed]
256. Zhang, X.-Y.; Yu, Y.-S.; Chen, C.; Zhu, C.-C.; Yang, R.; Liu, Z.-J.; Liang, J.-F.; Chen, Q.-D.; Sun, H.-B. Point-by-point dip coated long-period gratings in microfibers. *IEEE Photonics Technol. Lett.* **2014**, *26*, 2503–2506. [CrossRef]
257. Xu, Z.; Li, Y.; Wang, L. Long-period grating inscription on polymer functionalized optical microfibers and its applications in optical sensing. *Photonics Res.* **2016**, *4*, 45–48. [CrossRef]
258. Derevyanko, S. Design of a flat-top fiber Bragg filter via quasi-random modulation of the refractive index. *Opt. Lett.* **2008**, *33*, 2404–2406. [CrossRef] [PubMed]
259. Yin, H.; Gbadebo, A.; Turitsyna, E.G. Top-hat random fiber Bragg grating. *Opt. Lett.* **2015**, *40*, 3592–3594. [CrossRef] [PubMed]

260. Xu, Y.; Lu, P.; Gao, S.; Xiang, D.; Mihailov, S.; Bao, X. Optical fiber random grating-based multiparameter sensor. *Opt. Lett.* **2015**, *40*, 5514–5517. [CrossRef] [PubMed]
261. Xu, Y.; Gao, S.; Lu, P.; Mihailov, S.; Chen, L.; Bao, X. Low-noise Brillouin random fiber laser with a random grating-based resonator. *Opt. Lett.* **2016**, *41*, 3197–3200. [CrossRef] [PubMed]
262. Kumar, A.; Varshney, R.K.; Sharma, P. Transmission characteristics of SMS fiber optic sensor structures. *Opt. Commun.* **2003**, *219*, 215–219. [CrossRef]
263. Tripathi, S.M.; Kumar, A.; Varshney, R.K.; Kumar, Y.B.P.; Marin, E.; Meunier, J.-P. Strain and temperature sensing characteristics of single-mode–multimode–single-mode structures. *J. Lightwave Technol.* **2009**, *27*, 2348–2356. [CrossRef]
264. Wang, P.; Brambilla, G.; Ding, M.; Semenova, Y.; Wu, Q.; Farrell, G. Investigation of single-mode-multimode-single-mode and single-mode-tapered-multimode-single-mode fiber structures and their application for refractive index sensing. *J. Opt. Soc. Am. B* **2011**, *28*, 1180–1186. [CrossRef]
265. Li, L.; Xia, L.; Xie, Z.; Liu, D. All-fiber Mach-Zehnder interferometers for sensing applications. *Opt. Express* **2012**, *20*, 11109–11120. [CrossRef] [PubMed]
266. Li, Z.; Wang, Y.; Liao, C.; Liu, S.; Zhou, J.; Zhong, X.; Liu, Y.; Yang, K.; Wang, Q.; Yin, G. Temperature-insensitive refractive index sensor based on in-fiber Michelson interferometer. *Sens. Actuators B Chem.* **2014**, *199*, 31–35. [CrossRef]
267. Choi, H.Y.; Kim, M.J.; Lee, B.H. All-fiber Mach-Zehnder type interferometers formed in photonic crystal fiber. *Opt. Express* **2007**, *15*, 5711–5720. [CrossRef] [PubMed]
268. Coviello, G.; Finazzi, V.; Villatoro, J.; Pruneri, V. Thermally stabilized PCF-based sensor for temperature measurements up to 1000 °C. *Opt. Express* **2009**, *17*, 21551–21559.
269. Xu, Y.; Lu, P.; Song, J.; Chen, L.; Bao, X.; Dong, X. Dispersion effects of high-order-mode fiber on temperature and axial strain discrimination. *Photonics Sens.* **2015**, *5*, 224–234. [CrossRef]
270. Villatoro, J.; Monzón-Hernández, D. Low-cost optical fiber refractive-index sensor based on core diameter mismatch. *J. Lightwave Technol.* **2006**, *24*, 1409–1413. [CrossRef]
271. Wang, R.; Zhang, J.; Weng, Y.; Rong, Q.; Ma, Y.; Feng, Z.; Hu, M.; Qiao, X. Highly sensitive curvature sensor using an in-fiber Mach-Zehnder interferometer. *IEEE Sens. J.* **2013**, *13*, 1766–1770. [CrossRef]
272. Tian, Z.; Yam, S.S.; Loock, H.-P. Single-mode fiber refractive index sensor based on core-offset attenuators. *IEEE Photonics Technol. Lett.* **2008**, *20*, 1387–1389. [CrossRef]
273. Wong, W.C.; Chan, C.C.; Zhang, Y.F.; Leong, K.C. Miniature single-mode fiber refractive index interferometer sensor based on high order cladding mode and core-offset. *IEEE Photonics Technol. Lett.* **2012**, *24*, 359–361. [CrossRef]
274. Chen, J.; Zhou, J.; Jia, Z. High-sensitivity displacement sensor based on a bent fiber Mach-Zehnder interferometer. *IEEE Photonics Technol. Lett.* **2013**, *25*, 2354–2357. [CrossRef]
275. Mao, L.; Lu, P.; Lao, Z.; Liu, D.; Zhang, J. Highly sensitive curvature sensor based on single-mode fiber using core-offset splicing. *Opt. Laser Technol.* **2014**, *57*, 39–43. [CrossRef]
276. Zhou, J.; Wang, Y.; Liao, C.; Sun, B.; He, J.; Yin, G.; Liu, S.; Li, Z.; Wang, G.; Zhong, X. Intensity modulated refractive index sensor based on optical fiber Michelson interferometer. *Sens. Actuators B Chem.* **2015**, *208*, 315–319. [CrossRef]
277. Cui, W.; Si, J.; Chen, T.; Hou, X. Compact bending sensor based on a fiber Bragg grating in an abrupt biconical taper. *Opt. Express* **2015**, *23*, 11031–11036. [CrossRef] [PubMed]
278. Frazão, O.; Falate, R.; Fabris, J.; Santos, J.; Ferreira, L.; Araújo, F. Optical inclinometer based on a single long-period fiber grating combined with a fused taper. *Opt. Lett.* **2006**, *31*, 2960–2962. [CrossRef] [PubMed]
279. Lu, P.; Chen, Q. Asymmetrical fiber Mach-Zehnder interferometer for simultaneous measurement of axial strain and temperature. *IEEE Photonics J.* **2010**, *2*, 942–953.
280. Yin, G.; Lou, S.; Zou, H. Refractive index sensor with asymmetrical fiber Mach-Zehnder interferometer based on concatenating single-mode abrupt taper and core-offset section. *Opt. Laser Technol.* **2013**, *45*, 294–300. [CrossRef]
281. Lu, P.; Chen, Q. Femtosecond laser microfabricated fiber Mach-Zehnder interferometer for sensing applications. *Opt. Lett.* **2011**, *36*, 268–270. [CrossRef] [PubMed]
282. Zhao, Y.; Li, X.-G.; Cai, L. A highly sensitive Mach-Zehnder interferometric refractive index sensor based on core-offset single mode fiber. *Sens. Actuators A Phys.* **2015**, *223*, 119–124. [CrossRef]

283. Zhang, S.; Zhang, W.; Gao, S.; Geng, P.; Xue, X. Fiber-optic bending vector sensor based on Mach-Zehnder interferometer exploiting lateral-offset and up-taper. *Opt. Lett.* **2012**, *37*, 4480–4482. [CrossRef] [PubMed]
284. Qi, T.; Xiao, S.; Shi, J.; Yi, L.; Zhou, Z.; Bi, M.; Hu, W. Cladding-mode backward-recoupling-based displacement sensor incorporating fiber up taper and Bragg grating. *IEEE Photonics J.* **2013**, *5*, 7100608.
285. Fan, J.; Zhang, J.; Lu, P.; Tian, M.; Xu, J.; Liu, D. A single-mode fiber sensor based on core-offset inter-modal interferometer. *Opt. Commun.* **2014**, *320*, 33–37.
286. Sun, H.; Yang, S.; Zhang, X.; Yuan, L.; Yang, Z.; Hu, M. Simultaneous measurement of temperature and strain or temperature and curvature based on an optical fiber Mach-Zehnder interferometer. *Opt. Commun.* **2015**, *340*, 39–43. [CrossRef]
287. Li, C.; Ning, T.; Zhang, C.; Wen, X.; Li, J.; Zhang, C. Liquid level and temperature sensor based on an asymmetrical fiber Mach-Zehnder interferometer combined with a fiber Bragg grating. *Opt. Commun.* **2016**, *372*, 196–200. [CrossRef]
288. Wang, Q.; Kong, L.; Dang, Y.; Xia, F.; Zhang, Y.; Zhao, Y.; Hu, H.; Li, J. High sensitivity refractive index sensor based on splicing points tapered SMF-PCF-SMF structure Mach-Zehnder mode interferometer. *Sens. Actuators B Chem.* **2016**, *225*, 213–220. [CrossRef]
289. Zhao, Y.; Li, X.-G.; Cai, L.; Yang, Y. Refractive index sensing based on photonic crystal fiber interferometer structure with up-tapered joints. *Sens. Actuators B Chem.* **2015**, *221*, 406–410. [CrossRef]
290. Konidakis, I.; Konstantaki, M.; Tsibidis, G.D.; Pissadakis, S. Light driven optofluidic switch developed in a ZnO-overlaid microstructured optical fiber. *Opt. Express* **2015**, *23*, 31496–31509. [CrossRef] [PubMed]
291. Consales, M.; Pisco, M.; Cusano, A. Lab-on-fiber technology: A new avenue for optical nanosensors. *Photonics Sens.* **2012**, *2*, 289–314. [CrossRef]